Università degli studi di Padova

Dipartimento di Fisica e Astronomia

Tesi magistrale in Fisica

Light-induced phenomena in droplets generated by opto-microfluidic lithium niobate platforms

Relatore:
Cinzia Sada
Correlatore:
Riccardo Zamboni
Controrelatore:
Gianpaolo Mistura

Laureando:
Lea Pennacchioni

Abstract

Since the advent of microfluidics approximately two decades ago, there has been a steady increase in the interest and development of tools for fluid flow at the microscale. Microfluidic technology's success is due to the fact that the volume of reagents can be significantly reduced from milliliters and microliters to nanoliters and femtoliters with a consequent reduction of the time needed to perform typical laboratory operations.
One subcatagory of microfluidics is droplet-based microfluidics, where discrete volumes are created using immiscible liquinds.
In particular the combination of microfluidics and integrated fast analysis tools allow the realization of Lab-On-a-Chip (LOC) devices, able to perform laboratory analysis where facilities themselves lack.

In this work of thesis a LOC prototype prototype for both the generation and the detection of droplets, completely integrated in lithium niobate is presented. The device is composed of an array of optical single mode waveguides coupled with a microfluidic stage, where water-in-oil droplets are produced in cross-flowing thanks to a passive droplet generator, a T-junction. Droplets flowing inside the microfluidic channel are detected using a laser light trasmitted in the optical waveguide and recorded by a tailored electronic circuit. The optical signal of a droplets is characterized by a complex dynamic trend which presents characteristic fingerprints related to the properties of the droplet, such as its shape. The transmittivity analysis of the droplets is very complicated due to refractivity and diffraction phenomena, it is therefore mandatory to study, at least phenomenologically, the shape of the signal and to associate it to some reliable parameters. These parameters must be related to informations coherent with the physical characteristics of the droplet.
In particular the parameters considered are: the integral of the signal which gives informations on the curvature of the droplet; the minimum of the droplet which is representative of the trasmittivity of the signal and can be used to deduce the shape of the dropet; the time taken by the droplet to

pass in front of the waveguide, which is linked to the length of the droplet and the left and right integrals which are used to deduce the symmetry of the droplets. In this work of thesis the analysis of this parameters as a function of the flow rate $\phi = Q_{water}/Q_{oil}$ was performed over a wide range of ϕ, covering the microfluidic squeezing and squeezing-to-dripping regimes. In particular the experiments were carried out fixing the falue of the water flux while varying the flux of the oil. Measurements varying the viscosity of the water, by creating glycerol-water solutions were also performed using the same protocol.

Contents

Introduction

Microfluidic technology holds great promise as it can perform typical laboratory applications using a fraction of the volume of reagents in significantly less time. Although it was originally developed for ink-jet printing, it has been widely applied in biotechnology [21][27] and in micro-analytical chemistry [28] because reagents can be strongly reduced from millilitres and microliters to nanolitres and femtolitres whereas hours of reaction time could be decreased to mere seconds or less [27]. Thanks to its scalability and parallel processing, the droplets microfluidics has been therefore used in a wide range of applications [29] including the synthesis of biomolecules, drug delivery and diagnostic testing and bio-sensing [30] as well as chemical kinetics studies and photochemical investigations. Although the continuous flow devices offer fine control over flow characteristics, scaling up is a challenge as the size of devices scales almost linearly with the number of parallel experiments. Independently of the application, instead, droplet microfluidics allows to generate a large number of droplets, each being a micro-system (i.e a micro-reactor), where potentially a a large number of reactions can be perfomend in parallel without increasing device size or complexity [25]-[26]. Moreover, due to the high surface area to volume ratios at the microscale, heat and mass transfer times and diffusion distances are shorter, facilitating faster reaction times. Unlike continuous-flow systems, droplet-based microfluidics allows also for independent control of each droplet, thus generating micro-reactors that can be individually transported, mixed, and analysed [28]. Finally, depending on the flow parameters and the channels geometry, it is possible to produce a rich and complex scenario of stable droplets patterns and even more complicated geometries where core-shell droplets can be designed. Although the high potentialities of droplet microfluidics are still increasing, a key point in its real efficient exploitation relies on the control of the droplets size distribution and its relative monitoring. Different methods have been devised that produce highly monodisperse droplets in the nanometer to micrometer diameter range, at rates of up to twenty thousand per second [31] but the analysis of its monodispercity is still mainly perfomed by the ex-

ploitation of imagining techniques by way of microscope coupling. Within the widespread applications of droplet microfluidics, novel micro-fabrication techniques are continuously being developed ([32], [33]) to optimise the monidispesity character. They exploit a variety of materials including polymers and glass as substrates to realize the microfluidic circuit. Further stages such as those required for the fluid pumping and sorting and for the optical analysis are commonly realized by using external equipments. In particular the incorporation of chemical and physical sensors perfectly integrated with the microfluidic circuit is still under debate [34], although the optical methods are the most used. One of the main reasons of the lack of integration is due to the fact that the most commonly used materials like PDMS and glass complicate the full integration of the fluidic and optical functionalities in the same substrate. In this scenario, the integration of a large number of different stages on a single substrate chip is a key point for promoting new insights in many applications that need portable devices to speed the analysis and allow investigation of new phenomena [35], [36]. In this frame of reference, the possibility to combine optics functionalities and microfluidics has gained great interest and is nowadays referred opto-microfluidics, especiually for those which can integrate monitoring systems of the droplets generation and their quality. Opto-microfluidics consists of integrating microfluidic and microphotonic components onto the same platform, where fluid and light are driven to interact. This combination offers new opportunities for a large variety of applications [38]-[39]: among the others, effective compact bio-sensors have attracted great attention because they combine the high sensitivity of micro-photonic devices to the properties of small amounts of fluids that surround them [40]-[41]. Recently self-calibration systems to be directly coupled to the microfluidic systems have been addressed as a core business in the perspective of delivering a portable opto-miriofluidics final device. On this basis, the lab-on-a-chip technology, the optofluidic integrations represent a further development of the lab-on-a-chip technology [42]: this has actually driven most of the current works and efforts for integrating the optical devices that are usually implemented in biological and chemical detection schemes (like optical light sources and photodetectors) onto compact and planar optofluidic platforms [43]: in this field, the incorporation of chemical and physical sensors perfectly integrated with the microfluidic circuit is under debate [44] as well as the possibility of monolithical integration is still far from being available. Among all the characteristics required to optofluidic integration, compactness and tunability were addressed as key features to achieve a high degree of functionality and large-scale integration. A broad range of highly flexible optofluidic devices were therefore presented to bring new tools in integrated optics applications, like tunable attenu-

ators, optofluidic lasers and light sources, tunable filters, optical switches and tunable interferometers [45]-[46]. In parallel, a novel class of optically controlled photonic devices were also demonstrated to optically manipulate micronscale dielectric objects within fluid environment through tightly focused laser beams, such as optical tweezers and stretchers, as well as traps and sorters that were applied: in this case, the micro-elements were mainly microspheres, tapered fibers and biological targets as cells. In most cases the proposed devices exploited hydrid configurations and were designed to provide only one specific investigation such as mechanical response of the target upon stretching [47]-[?] target movement in given direction to get sorting being the most wide-spread, with taget tracing by way of imaging techniques [49]. In this scenario, the integration of a large number of different stages on a single substrate chip is a key point for promoting new insights in many applications that need portable devices to speed the analysis and allow investigation of new phenomena [[?]-[60]]. Among the others, lithium niobate (LiNbO3) crystals have been proposed in microfluidics application since it demonstrated to be bondable to other polymeric materials and allows for high efficient surface acoustic waves (SAW) generation to move droplets on the substrate in a very controlled way. Recently, in fact, micro-pumps based on the piezoelectric properties of LiNbO3 have been reported to move the liquid in a closed square loop channel and flow mixing, pyroelectric and photogalvanic particle trapping [[52]] were proposed. Quite surprisingly, all the above mentioned applications were realized without producing a microfluidic circuit directly on LiNbO3 substrates (apart from [67]-[71]) and without the integration of optical sensing stages or complex multifunctionals platform although it is a material thoroughly exploited in the photonic and integrated optics industry. As a matter of fact lithium niobate can host high quality optical waveguides and complex devices such as multiplexer, switch and optical modulators are commercially available thanks to its high wide transparency (75% from 350-3450 nm): the Ti in – diffusion technique [?] is routinely employed together with standard photolithography for the production of optical circuit as well as ion implantation [65]. Morover, diffractive optical elements, such as gratings, were designed exploiting its photorefractive effect (i.e a suitable inhomogeneous illumination induces in the material a correlated modification in the refractive index due to the electro-optic effect) [66]. This property is strongly enhanced by local doping with metal impurities with two valence states such as iron and copper [55]. Up to now the investigation on this field was mainly focused on bulk doped $LiNbO_3$ crystals but, recently, the interest in the local doping has been increasing thanks to its versatility and integration with other optical functionalities. In this thesis the attention was focused on the study of the physical response of an

opto-microfluidic where a set of droplets generated in a suitalble microfluidics circuit are properly illuminated by integrated optical waveguides crossing the microfluidic channels resepctively. This study is of paramount importance to identify the fluid nature, the size and volume of the droplets in order to deliver an analysis tool of the droplets size distribution without the exploitation of imagining techniques and microscope coupling. In order to reach this aim, in this thesis severl fingerprints of the droplets passage were carefully investigated and correlated to the droplets geometrical shape to give a set of markers representatives of the droplet itself with a perspective to generate, monitor and analyse more complicated systems such as those made of core-shell configurations.

Chapter 1

Microfluidic platforms in Lithium Niobate

In this work of thesis a Lab-on-a-Chip prototype for both generation and detection of droplets, completely integrated in lithium niobate is presented. The main idea is to develop and anlaysis stage to identify and detect droplets in a multiarray configuration. In particular it comprehends an array of optical waveguides perpendicularly to a microfluidic channel in order to perform an optical analysis of the droplets flowing therein.
In this chapter lithium niobate will be presented outlining its compositional, piezoelectric, pyroelectric and optical properties. A particular attention is devoted to the properties which could be employed in the field of optofluidics, a research area where lithium niobate is a quite unexplored material. The second section of the chapter will be dedicated to a brief explanation of droplet microfluidics, in particular to the description of the theoretical models describing the behavior of the T-junction droplet generators, which are used in the microfluidic stage of the Lab-on-a-Chip presented here.
The final part of the chapter will be addressed to the realization of microfluidic channels engraved in lithium niobate. In particular mechanical dicing technique will be presented together with the characterization of the microfluidic channels obtained by means of this technique. The techniques employed to close the channels will be also described. Finally a wettability study of lithium niobate and a functionalization process to increase its hydrophobicity will be presented.

1.1 Lithium Niobate

Lithium niobate was described for the first time by Zachariasen in 1928 and then widely investigated by Nassau and Abrahams at Bell Laboratories in the sixties. It is a solid, transparent material not soluble in water and organic solvents. It is a synthetic material therefore cannot be found in nature. It is a compound of the pseudo-binary system $Li_2ONb_2O_5$, besides $Li_2Nb_{28}O_{71}$,Li_3NbO_4 and the lithium triniobate $LiNb_3O_8$. The crystal is usually grown by Czochralski technique in its *congruent* composition which is characterized by a lithium deficiency (48.45% of Li_2O). This composition corresponds to a maximum in the liquid-solid curve as depicted in the phase diagram in 1.1. At the congruent composition the melting and the growing

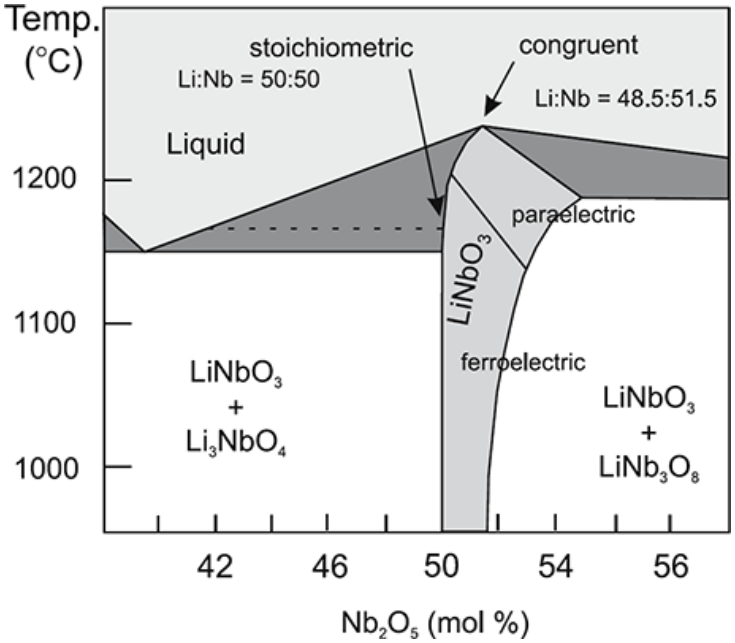

Figure 1.1: Phase diagram of $LiNbO_5$.[2]

of the crystal are identical with respect to the composition, so these crystals show the highest uniformity of the their chemical and physical properties (differently from a stoichiometric crystal where the composition of the melt and the crystal are slightly varying during the growth and the crystal becomes non-uniform, particularly along the growth axis). Several physical and optical properties, like the phase transition temperature, the birefringence, the photovoltaic effect and UV band absorption edge, strongly depend on the ratio between the concentration of lithium and that of niobium ratio [1].
This is why the congruent composition is preferred and stoichiometric wafers

are not available in commerce at low prices. At room temperature a $LiNbO_3$ crystal exhibits a mirror symmetry about three planes that are 60^o apart. The axis obtained by their intersection is the center for a three-fold rotational symmetry of the crystal. These symmetries classify the lithium niobate as a member of the space group $R3c$, with point group $3m$. Above the transition temperature it belongs to the centrosymmetric space group $R3m$. In the trigonal system the definition of the crystallographic axes is not unambiguous and three different cells can be chosen: hexagonal, rhombohedral or orthohexagonal.

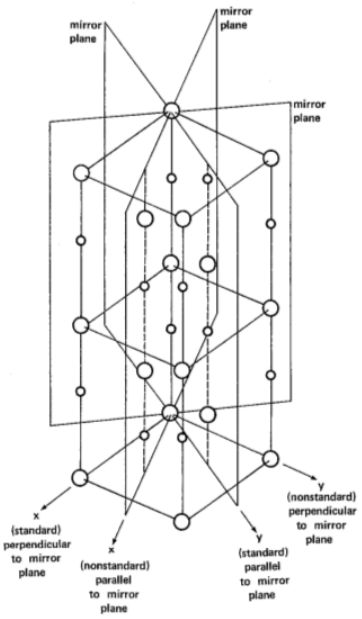

Figure 1.2: Lithium niobate three plane symmetry elements.

In most applications the orthohexagonal is preferred and usually the tensor components describing lithium niobate physical properties are expressed with respect to the axes from this picture. Nevertheless in crystallography applications the other two descriptions are used as well. The three mutually orthogonal reference axes in the orthohexagonal convention are:

- the z-axis (also indicated as c-axis or optical axis) which is the axis around which the crystal exhibits its three-fold rotation symmetry;
- the y-axis, which lays on the mirror plane;
- the x-axis, perpendicular to the previous ones.

In particolar, given the fact that the piezoelectricity is proper of z-axis and y-axis, by convention their positive direction is chosen to be pointing on the negatively charged plane under uniaxial compression. Due to the crystal pyroelectricity along the optical axis, z-axis direction is also indicated as that pointing to the positively charged plane while the crystal is cooling. Commercial wafers from Crystal Technology employed during the work for this thesis have facets along the circular border at specific directions in order to be easily oriented. Lithium niobate structure at temperatures below its ferroelectric Curie temperature ($T_C = (1142.3 \pm 0.7)^oC$ for congruent composition) consists of planar sheets of oxygen atoms in a slightly distorted hexagonal close-packed configuration. The octahedral interstices formed by this oxygen structure are one-third filled by lithium atoms, one-third by niobium and one third is vacant, following, along the c-axis, the order Li- Nb-vacancy. In the paraelectric phase, above the Curie temperature, the lithium atoms lie in the oxygen layers, while niobium ions are located at the center of oxygen octahedrals (see Fig.1.3) The paraelectric phase has no dipolar moment. On

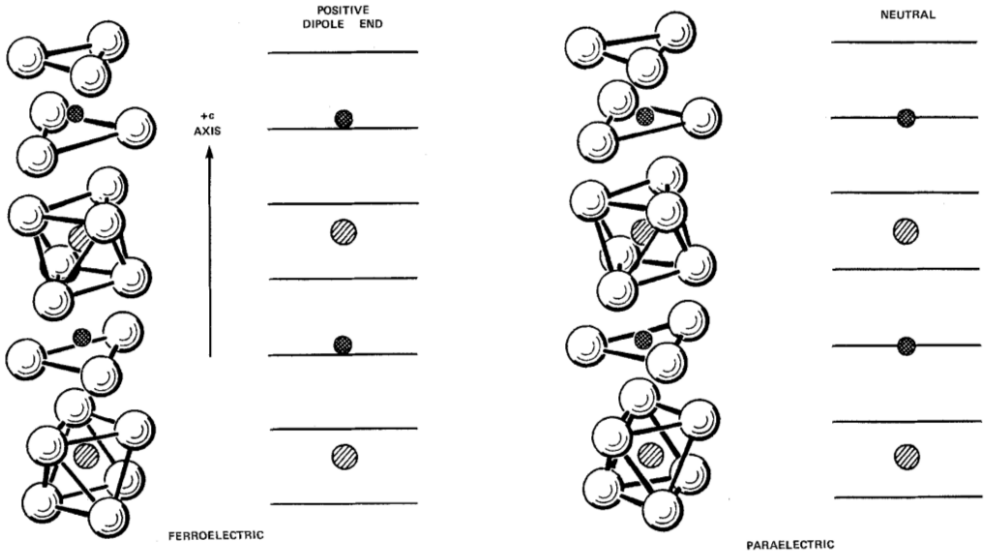

Figure 1.3: Compositional structure of $LiNbO_5$ and sketch of lithium and niobium athoms with respect to the oxygen planes in the paraelectric phase (right) and the ferroelectric phase(left).

the contrary, as the temperature decreases below T_C , lithium and niobium atoms are forced into new positions: the Li ions are shifted with respect to the O planes by about 44 pm, and the Nb ions by 27 pm from the center of the octahedra. These shifts cause the arising of a spontaneous polarization, causing the $LiNbO_3$ to belong to the class of displacement ferroelectrics.

1.1.1 Defects and doping

Impurities and structural modifications are extremely important in the study of lithium niobate since they can modify considerably its physical properties. As mentioned before congruent lithium niobate has a sub-stoichiometric fraction of lithium which corresponds to the lack of about the 6% of lithium atoms compared to the stoichiometric composition. Structure modifications are thus needed to ensure charge compensation after Li_2O outdiffusion. Three different models have been proposed:

- **oxygen vacancy model** : when lithium oxide outdiffusion is compensated by oxygen vacancies as it usually occurs in the oxides perovskites

$$\langle LiNbO_3 \rangle \longrightarrow 2V_{Li} + VO_2^- + Li_2O$$

- **lithium vacancy model** : when some of the lithium vacancies are compensated by niobium atoms (niobium antisites)

$$\langle LiNbO_3 \rangle \longrightarrow 4V_{Li}^- + Nb_{Li}^{4+} + 3Li_2O$$

- **niobium vacancy model** : when both niobium vacancies and niobium antisites concur to reach compensation

$$\langle LiNbO_3 \rangle \longrightarrow 4V_{Nb}^{5+} + 5Nb_{Li}^{4+} + 3Li_2O$$

The question on which mechanisms prevail is still under debate but the oxygen vacancy model seems to be disproved by density measurements [3] which instead confirms the hypothesis of niobium antisites. This substitutional niobium atoms are important since they introduce donor and acceptor levels in the bandgap of the stoichiometric crystal giving rise to the photovoltaic and phtorefractive effect even in the absence of extrinsic impurities.
Since the sixties extrinsic defects have been employed to tailor lithium niobate properties. Lithium niobate doping is quite straightforward, due to its high concentration of vacancies. Dopants can be added both during the crystal growth or after the solidification by thermal diffusion or ion implantation. Extrinsic defects are used both to enhance or reduce the photorefractive effect: Fe on one hand, Mg, Zr, Zn and Hf on the other hand. Titanium by thermal in-diffusion and hydrogen by proton exchange are used to produce optical waveguides on the surface of the crystal. Erbium doping was also exploited in order to realize integrated laser sources[4].

1.1.2 Physical Properties

The coordinate system used to describe the physical tensor properties of lithium niobate is a Cartesian x,y,z system, where the z axix is chosen to be parallel to the c axis, the x axis is chosen to coincide with any of the equivalent a_H axis, and the y axis is chosen to be perpendicular to x, z so that the system is right handed. Fig.1.2 shows both the standard convention and a secondary convention for choosing x, y principal axis within the hexagonal unit cell.

Under compression the $+y$ face becomes negatively charged.

Optical Properties

Pure lithium niobate is a quite transparent crystal presenting a negligible absorption coefficient from 0.35 μm to about 5 μm. Light absorption coefficient is very sensitive to the presence of defects or impurities while light propagation is weakly affected by scattering (the extinction coeffcient being 0.16 dB/cm). Due to the crystallographic structure and the symmetry properties of lithium niobate, its permittivity tensor, in the orthohexagonal cell reference framework, can be represented by a 3×3 matrix with the form:

$$\epsilon = \begin{pmatrix} \epsilon_{11} & 0 & 0 \\ 0 & \epsilon_{11} & 0 \\ 0 & 0 & \epsilon_{33} \end{pmatrix} \tag{1.1}$$

The anisotropy of the permittivity tensor lead to the characteristic birefringence of lithium niobate. In fact two different refractive indices can be found in lithium niobate: the ordinary refractive index n_o (for electromagnetic waves plarized perpendiculary to the z-axis of the crystal) and the extraordinary refractive index n_e (wave with a polarization parallel to the optical axis). The two refractive indeces can be written in terms of the two coefficients ϵ_{11}, ϵ_{33} as:

$$n_o = \sqrt{\frac{\epsilon_{11}}{\epsilon_0}}; \qquad n_e = \sqrt{\frac{\epsilon_{33}}{\epsilon_0}}.$$

Refractive indices dependence on light wavelength and crystal composition can be inter- polated by the generalized Sellmeier equation, which is valid in the wavelength range $\lambda = 400 \div 3000\ nm$ and for compositions of $C_{Li} = 47 \div 50\ mol\%$ to an accuracy of 0.002 in n_i:

$$n_i^2 = \frac{A_{0,i} + A_{1,i}(50 - C_{Li})}{\lambda_{0,i}^{-2} - \lambda^{-2}} + A_{UV} - A_{IR,i}\lambda^2 \tag{1.2}$$

where $i = e, o$ indicates either the ordinary or the extraordinary polarization; λ is the wavelength expressed in nanometers; A are intensity factors which describe the influence of various oscillators responable for the refractive indices in the visible and infrared region: A_0 for Nb on Nb site, A_1 for Nb in Li site, A_{UV} for plasmons, A_{IR} for phonons. The parameters at room temperature are listed in table 1.1.

Parameter	**Ordinary**	**Extraordinary**
A_0	$4.5312 \cdot 10^5$	$3.9466 \cdot 10^5$
A_1	$-4.8213 \cdot 10^8$	$79.090 \cdot 10^8$
A_{IR}	$3.6340 \cdot 10^8$	$3.0998 \cdot 10^8$
A_{UV}	2.6613	2.6613
λ_0	223.219	218.203

Table 1.1: Parameters for generalized Sellmeier equations at room temperature.

The typical refractive indices for a congruent composition at a wavelength of $\lambda = 632.8\ nm$, corresponding to a He-Ne laser, are:

$$n_o = 2.2866 \qquad n_e = 2.2028.$$

Apart on the Li/Nb ratio, lithium niobate refractive indices depend strongly on extrinsic impurities and this feature can be exploited to tailor n_o and n_e by doping.

Electro-optic Effect

The linear electro-optic effect is one of the most important features of lithium niobate crystals. It consists in the variation of the refractive index due to the application of an electric field according to the relation:

$$\Delta \left(\frac{1}{n^2} \right)_{i,j} = \sum_k r_{ijk} E_k + \sum_{k,l} s_{ijk} E_k E_l + ... \tag{1.3}$$

where $\Delta \left(\frac{1}{n^2}\right)_{i,j}$ is a second rank tensor describing the change in the relative permittivity, r_{ijk} is a third rank tensor describing the linear electro-optic effect while s_{ijk} a fourth-rank tensor describing the quadratic electro-optic

effect. Linear and quadratic electro-optic effects are usually called *Pockel effect* and *Kerr effect* respectively. In particular, in lithium niobate the Kerr effect can be neglected since it has been observed to be significant only under and applied electric field above 65 kV/mm. Due to its symmetry lithium niobate electro-optic linear coefficients can be expressed as a reduced tensor[1]:

$$r = \begin{pmatrix} 0 & -r_{22} & r_{13} \\ 0 & r_{22} & r_{13} \\ 0 & 0 & r_{33} \\ 0 & r_{42} & 0 \\ r_{42} & 0 & 0 \\ -r_{22} & 0 & 0 \end{pmatrix} \tag{1.4}$$

According to the measurements reported by Bernal et al.[6] the values for this coefficients are $r_{13} = 8.6{\cdot}10^{-12}\, m/V$, $r_{22} = 3.4{\cdot}10^{-12}\, m/V$, $r_{33} = 30.8 \cdot 10^{-12}\, m/V$, $r_{51} = r_{42} = 28.0 \cdot 10^{-12}\ m/V$.
Electro-optic effect is a key-point for integrated optics applicatios since together with titanium in-diffused waveguides it can be used to realize optical modulators and switches. This characteristic grows the number of possibilities also in optofluidic applications and makes lithium niobate a better choice than other materials such as silica where waveguides are possible but no electro-optic effect is present.

Piezoelectricity

It is also possible to induce a polarization in lithium niobate with an applied stress. This phenomenon is called piezoelectricity. In particular the induced polarization is:

$$P_i = \sum_{j,k} d_{ijk}\sigma_{jk} \tag{1.5}$$

where σ is the second-rank symmetric stress tensor and d is the third-rank piezoelectric tensor. The stress tensor has six independent components since $\sigma_{ij} = \sigma_{ji}$. Moreover the crystal symmetry implies a further reduction of the d independent components. The result is a piezoelectric tensor d with four independent components which can be expressed in the reduced notation as:

$$d_{ijk} = \begin{pmatrix} 0 & 0 & 0 & 0 & d_{15} & -2d_{22} \\ -d_{22} & d_{22} & 0 & d_{15} & 0 & 0 \\ d_{31} & d_{13} & d_{33} & 0 & 0 & 0 \end{pmatrix} \tag{1.6}$$

[1]The convention jk=11$\longrightarrow$1, jk=22$\longrightarrow$2,jk=33$\longrightarrow$3, jk=32,23$\longrightarrow$4,jk=1331$\longrightarrow$5, jk=1221$\longrightarrow$6 has been used.

Piezoelectric crystals also exhibit the converse piezoelectric effect(generation of stress when an electric field is applied). In tensor component form, the converse piezoelectric effect can be expressed as:

$$S_{ik} = \sum_i d_{ijk} E_i \tag{1.7}$$

where S_{ik} is thesecond-rank strain tensor.

Pyroelectric Effect

A pyroelectric solid exhibits a change in spontaneous polarization as function of temperature. The relationship between the change in temperature, ΔT, adn the change in the spontaneous polarization, ΔP, is linear and can be written as $\Delta P = p\Delta T$, where p is the pyroelectric tensor. In lithium niobate this effect is due to the movement of the lithium and niobium ions relative to the oxygen layers. Since these ions only move in a direction which is parallel to the c-axis, the pyroelectric tensor component is of the form,

$$p_i = \begin{pmatrix} 0 \\ 0 \\ p_3 \end{pmatrix} \tag{1.8}$$

where $p_3 = -4 \cdot 10^{-5} C/(K - m^2)$.

Photovoltaic effect

The bulk photovoltaic effect of lithium niobate was discovered in 1974 by Glass et al., who observed that a stationary current rises after the crystal was exposed to light. This is a typical effect of non-centrosymmetric crystals by which the momentum of the photo-excited electrons has a preferential direction, resulting in a current density:

$$j_{phv,i} = \beta_{ijk} e_j e_k^* I = \alpha k_{G,ijk} e_j e_k^* I \tag{1.9}$$

where e_j and e_k are the polarization vectors of the incident light wave, I is the intensity of the incident light wave and β_{ijk} are the components of a third rank tensor called photovoltaic tensor, which can be expressed as $\beta_{ijk} = \alpha k_G$ where α is the absorption coefficient and k_G is the Glass coefficient. In lithium niobate only four components of the photovoltaic tensor are independent: $\beta_{333}, \beta_{311} = \beta_{322}$, $\beta_{222} = -\beta_{112} = \beta_{121}$ and $\beta_{113} = \beta_{131}^* = \beta_{232} = \beta_{223}^*$. The generated current density is mainly directed along the optical axis of the crystal as $k_{G,333} = 2.7 \cdot 10^{-9} cm/V$ and $k_{G,322} = 3.3 \cdot 10^{-9} cm/V$ while the generated current along the y-axis is one orer lower in magnitude.

1.2 Microfluidics in Lithium Niobate

Microfluidics is the research field that studies, controls and manipulates the dynamics of extremely small amounts of fluids (from milliliters to femtoliters), flowing inside confined geometries with characteristic lenghts (in the order of tens of microliters of less). Due to the small dimensions of the microchannels, microfluidic devices are characterized by low values of the Reynolds number

$$Re = \frac{\rho \mu L}{\eta} \tag{1.10}$$

usually much less the 100. In this Reynolds number regime the flow is completely laminar and no turbolence occurs (the transition to the turbolent flow generally occurs in the range of $Re \sim 2000$).
Moreover, microfluidics provides an extremely steady control on the manipulated samples and a very low reagents consumption. For these reasons, since its birth in the 1950s, it has been employed in a wide range of applications: from chemical synthesis to information technology, from biological analysis to drug delivery.

One subcathegory of microfluidics is droplet based microfluidics which involves the generation and manipulation of discrete droplets inside microdevices.
The main motivation behind the field of microfluidics is to create Lab-on-a-Chip (LOC) devices. The idea behind a LOC is to transfer all laboratory functionalities into a small portable device. In particular many micro-devices have been already realized which are able to pull the fluids inside the channels, to manipulate small amounts of liquids, to mix and merge them, to catch and sort particles dispersed in the fluids, to perform analyses of diluted species and many others. Despite the many accomplishments the integration of all these stages in order to realize a single multi-purpose micro-device which gets rid of all external macro add-ons it is still a challenge. In fact what is hardly highlighted in microfluidics applications is that although a multitude of micro-devices manipulating nanolitres droplets have been realized, they usually need macro syringe pumps or pressure controllers to operate and usually the analysis is carried out putting the chip under the objective of a "big" microscope.

1.2.1 Droplet Microfluidics

Unlike continuous flow systems, droplet-based systems focus on creating discrete volumes with the use of immiscible phases. The main idea is to confine the fluid of interest (which would be the one containing chemical reagents, molecules or biological samples) inside droplets surrounded by another immiscible fluid phase used to carry droplets along the microfluidic channels. The fluid that makes up the droplets is generally called *dispersed phase* while the outer fluid surrounding the droplet is called *continuous phase*.
There are several techniques to produce droplets inside a microfluidic channel. The main requirement for any of them is the high reproducibility and the low volume distribution dispersion. Other common targets to be achieved are a high production frequency, the possibility of produce steady droplet in a wide range of volume, the versatility deriving from the possibility of employing the same device with different liquids and the simplicity of its usage. Droplet generation methods can be divided in two categories:

- **passive methods**: are based on the interaction between the two immescible fluids constrained in a confined geometry. The generation of the droplets does not require any contribution from specific energy sources. The properties of the droplets (such as size and shape) are tailored by the control of the inlet fluxes of the injected fluids. These methods are based on the realization of accurate geometry designs of the microfluidic channels; on a suitable choice of the fluids employed and on a selected wettability of the channels materials.

- **active methods:** need the exploitation of an external source of energy for the generation of the droplets.

In this work of thesis a passive production method was used as it represents the simplest way to produce droplets with high control on their volume. Therefore in the following a more detailed description of passive methods will be presented while active methods will not be mentioned. However it worth mentioning that one of the most interesting perspective of the employment of lithium niobate as a substrate for microfluidics is indeed the possibility of a complete integration due to its peculiar properties such as its piezoelecricity, piroelectricity, photorefrativity...

All passive methods require the control on the fluxes of the contiunuous phase Q_c and the dispersed phase Q_d or, alternatively, on their inlet pressures p_c and p_d. The most important feature of a passive droplet generator is the geometry of the channels near the region where droplets are produced. Thus a first classification of droplet generators can be made based on the nature of flow field near pinchoff. Fig1.4 showes a scheme of the three main configurations: co-flowing, flow-focussing and cross-flowing.

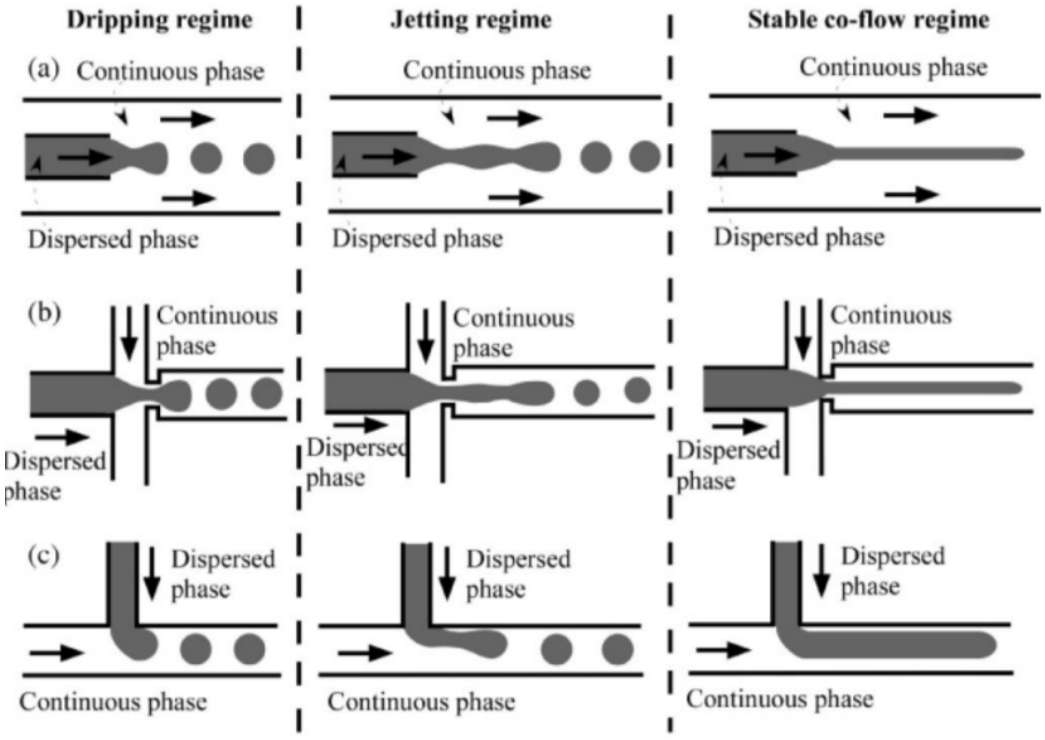

Figure 1.4: Droplet generation types: (a) co-flowing; (b) flow-focusing; (c) cross-flowing. Three typical operation regimes are shown from left to right: dripping, jetting and coflow.

- **Co-flowing configuration:** the geometry is characterized by two coaxial channels. The dispersed phase flows in the inner channel, while the continuous phase flows in the outer channel. When the dispersed phase emerges from the channel, after an initial stage where it flows together with the contiunuous one, the droplets are created by the Reyleigh-Plateau instability;
- **Flow-focusing configuration:** The channels are arranged in a cross and the continuous phase, shirnks the dispersed phase until the pinch-

off is reached. In this configuration an high stability over a wide range of droplet production frequencies is obtained;

- **Cross-flowing configuration:** The inlet channel containing the dispersed phase crosses at a wide angle the main channel where the contiunous phase is flowing. The dispersed phase obstructs the main channel interrupting the continuous phase stream before droplet break-up happens. Different geometries have been studied such as T-junctions, Y-junctions and multiple junctions.

As shown in Fig.1.4 the microfluidic devices can be operated at different regimes. These regimes depend on the physical properties of the fluids (such as the fluids densities ρ_c and ρ_d, viscosities μ_c and μ_d and interfaccial tension σ) or on parameters such as the fluids' fluxes Q_c and Q_d, and wettability properties such as the contact angle with the channel surfaces θ_c, θ_d. The three regimes shown in the scheme are:

- **Co-flowing:** the two phases flow parallel to each other and no droplets are formed.

- **Jetting:** after an initial unstable co-flowing thread, due to an instability the droplets are formed. This regime allows a fast production of small droplets, but has a wide volume dispersion.

- **Dripping:** The break-up takes place immediately, high frequency droplet production is possible in this regime.

The regimes described are the main flowing regimes, but another regime is possible, called *squeezing*, where the dispersed phase completely obstructs the main channel before droplet break-up occurs. It can be obtained for low values of Q_c and allows the production of larger droplets which entirely fill the channel, as shown in Fig.1.5.

In this work of thesis the microfluidic devices were operated in cross-flowing configuration (T-junction).

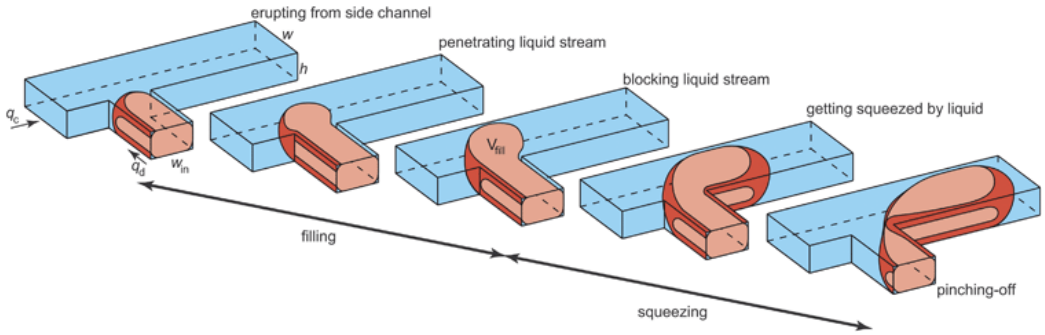

Figure 1.5: Formation of a droplet at a planar T-junction with height h. The formation cycle comprises two periods: a filling period in which the droplet fills-up the junction and grows to a size V_{fill} and a squeezing period in which the forming bubble is squeezed by the liquid until it pinches-off.

1.3 T-junction: A theoretical model

In a microfluidic T-junction, two immiscibile liquids flow into separate inlet channels that meet at right angles. The dispersed phase emerges into the junctions, and the cross-flow of the continuous phase deforms the emerging interface leading to break-up of discrete droplets.

In most cases both channels have the same heigth h but they may have different widths (w_c,w_d) which are normally set depending on the desired droplet dimension.
Droplets are produced thanks to the forces exerted by the continuous phase on the dispersed phase entering the main channel. In particular three main fluid stresses act on the emerging interface and influence the droplet breakup in a T-junction: viscous shear stress, interfacial tension and squeezing pressure.

When the dispersed phase starts to occupy a portion of the channel, the continuous phase is kept flowing in a narrower gap so it starts to flow faster and the pressure drop across the tip and the neck of the entering thread grows gradually. The effect is an increase in both the shear force, which is proportional to the continuous phase velocity, and the force driven by the pressure drop across the emerging droplet. The process ends as these forces overcome the capillary force which tends to keep the droplet attached to the dispersed phase thread so that the final result is the droplet break-up (Fig.1.5).

The regimes of dripping and squeezing normally used to produce droplets are characterized by a different balance between the mentioned forces. In particular, in the dripping regime the main contribution to droplet pinch-off

is given by the shearing viscous force. In the squeezing regime the break-up is driven by the pressure drop between the tip and the neck of the dispersed phase thread, since it obstructs the main channel increasing the resistance to the flow of the continuous phase.

An important parameter to distinguish between different regimes in microfluic confined geometries is the capillary number Ca which describes the relative magnitude of the viscous shear stress compared to with the capillary pressure. A simple definition for Ca is given in terms of the average velocity of the continuous phase u_c:

$$Ca = \frac{\eta_c u_c}{\sigma} = \frac{\eta_c Q_c}{\sigma w_c h} \tag{1.11}$$

Where η_c is the viscosity of the continuous phase, σ is the superficial tension, h and w_c are the height and the width of the microfluidic channel.
A precise description of the capillary number as a parameter to distinguish between the squeezing and dripping regimes was first provided by Garsteki *et al.*[18] and finally proved by the simulation of De Menech *et al.*[14], setting the critical value of separation between the two regimes at $Ca = 0.015$. For higher values of the capillary number the dripping regime is established as the viscous shear force dominates, while at smaller values of Ca the squeezing pressure is the dominant term and the squeezing regime is established.

As mentioned above, independently of the regime, droplets are produced by the main effect of three forces. The best fitting theory of the experimental data is the one provided by Christopher *et al.*. In the article an emerging dispersed phase thread is considered as sketched in Fig.1.6: the tip is depicted as a spherical shape with radius b connected to the dispersed phase by a neck with a width s which is $s = w_d$ at the beginning of the process.

As the author suggests, the breaking point starts when the three forces balance each other:

$$F_\sigma + F_\tau + F_p = 0 \tag{1.12}$$

The approximate for of every force is:

- **Capillary force F_σ :** given by the difference between the pressures at the upstream and downstream ends of the emerging droplet, multiplied by the area of the interface bh:

$$F_\sigma \sim \left[-\sigma\left(\frac{2}{b} + \frac{2}{h}\right) + \sigma\left(\frac{1}{b} + \frac{2}{h}\right)\right] bh = -\sigma h \tag{1.13}$$

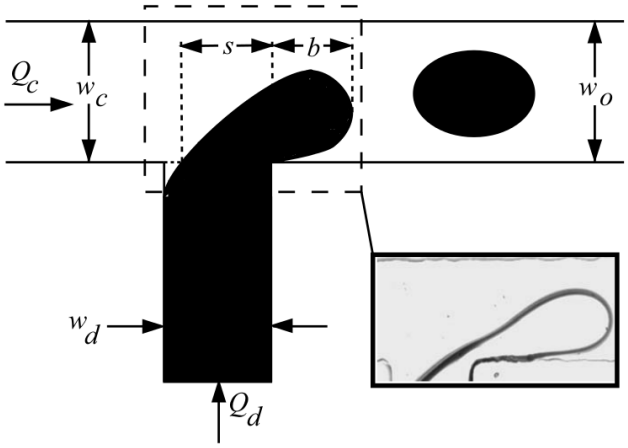

Figure 1.6: Schematic diagram of the emerging droplet.

- **Viscous shear force F_τ :** applied from the continuous phase flowing on the emerging dispersed phase. In the article the shear stress rate is approximated with the average velocity of the continuous phase u_c divided by the gap size between the wall and the tip of the droplet $(w_c - b)$:

$$F_\tau \sim \eta_c \frac{u_{gap}}{(w_c - b)} bh \sim \eta_c \frac{Q_c b}{(w_c - b)^2} \tag{1.14}$$

- **Squeezing pressure force F_p :** obtained from a lubrification analysis for the pressure-driven flow in a thin gap with aspect ratio $(w_c - b)/b$:

$$F_p \sim \Delta p_c bh \sim \frac{\eta_c u_{gap}}{(w_c - b)} \frac{b}{(w_c - b)} bh \sim \frac{\eta_c Q_c b^2}{(w_c - b)^2} \tag{1.15}$$

During the growth of the droplet, while b is approaching w c , the viscous shear stress and even more the squeezing pressure rise up till they overcome the capillary pressure opposing to droplet pinch-off. In dimensionless terms, the droplet size at the onset of the detachment is given by:

$$(1 - \bar{b})^3 = \bar{b} \cdot Ca \tag{1.16}$$

where $\bar{b} = b/w_c$.

So b is the droplet length achieved by the droplet before the neck starts to shrink under the push of the continuous phase.

The additional length gained by the droplet during the shrinking process can be readily obtained multiplying the droplet advancing speed $u_{growth} \sim Q_d/(bh)$ by the time needed to shrink the neck $t_{squeeze} \sim w_d/u_c \sim w_d w_c h/Q_c$, so that the final length rescaled on w_c results to be:

$$\bar{L} = \bar{b} + \frac{\Lambda}{\bar{b}}\phi \tag{1.17}$$

where$\bar{L} = L/w_c$, $\Lambda = \frac{w_d}{w_c}$ and $\phi = Q_d/Q_c$. With similar arguments the also the semi-empirical trend for the frequency (for a constant value of ϕ) was derived:

$$\bar{f} = \frac{\eta_c w_c f}{\sigma} \propto Ca^{1-\delta} \tag{1.18}$$

and the trends of the rescalated volume:

$$\bar{V} = \frac{V}{w_c^2 h} = \bar{L}\bar{b} = \bar{b}^2 + \Lambda\phi \tag{1.19}$$

which, for a fixed value of ϕ can be expressed in terms of Ca:

$$\bar{V} = \frac{\phi Ca}{\bar{f}} \propto Ca^{\delta} \tag{1.20}$$

1.3.1 Microchannel realization on Lithium Niobate

Although microfluidics was born in silicon transferring micro-fabrication techniques from electronics, nowadays the most employed materials for the realization of the channels are polymers such as PDMS(Polydimethylsiloxane) and PMMA (Poly(methyl methacrylate)). These materials' characteristics made polymer based microfluidics very promising for the realization of cheap throwaway devices for medical or biological applications.

On the other hand a fresh research field is growing in side of disposable microfluidics which has the aim to conceive durable multitasking integrated chips able to provide more sophisticated analyses and samples manipulation, requiring optical and electronic stages which cannot be realized on polymers and which are too expensive to rely on their poor durability.

Lithium niobate could be a valid alternative to glass and silicon for the integration of multiple stages able to produce, manipulate, sort droplets and analyze their contents. Many techniques have been employed for microfabrication on lithium niobate can be found in literature: chemical etching, reactive ion etching, foucused beam lithography, laser ablation and mechanical micromaching. The most important characteristics required is the optical quality of the lateral walls of the channels, necessary for the otical waveguides integration. However, in literature, the only attempts to engrave microfluidics channels directly on lithium niobate were presented in the last years by our colleagues at the University of France-Comté, Besançon (France) and by our group.

In particular the microchannels of the chip used in this work of thesis was realized by optical dicing with the DISCO DAD 321 dicing saw. The dicing saw used is a polimeric blade with diamond particles; its has a diameter of 56 mm and a thickness of 200 μm .

The parameters which allowed the best surface quality are the a rotation speed of 1000 rpm and a cutting speed of 0.2 mm/s. During the dicing a constant flow of water was used to keep the temperature low and to get rid of crystal residuals. The microchannels obtained were then characterized by optical microscopy with a Veeco Cp-II atomic force microscope (AFM) and by profilometry. The average roughness obtained is of approximately (19 ± 6) nm on the bottom surface and (6.8 ± 0.5) nm on the lateral surfaces. The natural geometry for the micromachining technique is a cross-junction with four branches, which is the geometry adopted for the creation of the chips in this work of thesis.

1.3.2 Chip sealing

Once the microfluidic channels have been engraved on the surface of the crystal, in order to complete the device it must be closed. The basic idea is to use a glass slide to act as top wall of the channel. The sealing process is a critical step as it is necessary to use a procedure that ensures a gas-tight covering without clogging the channels.

To glue the glass slide to the chip the Nordland Optical Adhesive 68 (NOA 68) by Norland Products Incorporation was used. It is a colourless, liquid photopolymer which solidifies after being exosed to UV light at a wavelength in the range of $(350 \div 380)\ nm$. The main steps of the sealing process are described in the following:

- four holes with a diameter of 2 mm were drilled on the glass slide at the end of the microfluidic channels;
- Four pieces of MASTERFLEX silicone tubing were placed over the holesand glues using Araldite bicomponent glue;
- the glass cover and the chip were then clamped together and a small amount of NOA68 was deposited all around the glass cover. During a period of time of about 24 hours the polymeric adhesive filled the thin space between the sample and the cover by capillarity reaching the microfluidic channels edges. Surface tension avoids NOA68 to flow inside the channels since they are much larger than the thin layer between the surfaces where NOA stays confined (100 μm of the channel height compared with the few microns of the gap between the crystal and the glass).
- The chip was then placed under an UV lamp for about 30 minutes, to cure definitely the layer.

1.3.3 Channels wettability and functionalization

One of the most important characteristic of a material which has to be employed in microfluidics applications is the wettability, i.e. the interaction between the fluids and the surface of the material. Wettability is the result of microscopic interactions between the surface and the molecules of the fluid and it usually depends on chemical composition and physical morphology of the surface, as well as on the chemical and physical properties of the fluid such as surface tension, molecules polarization and molecules polarizability.

In droplet microfluidics it is fundamental that the dispersed phase has a high contact angle while on the contrary the continuous phase should completely wet the solid.

The main aim of this work of thesis was the production of water droplets inside the microfluidc channels since, among the most interesting employments of optofluidics, biological applications seems to get the best acknowledgments and most of biological samples need to be dispersed in water solutions. The requirement for a continuous phase which is immiscible with water has a plenty of available solutions among oils. In this work the continuous phase was hexadecane with SPAN®80[2] (with a concentration of both 0.09% and 0.27%, both higher than CMC, which is 0.03 % for SPAN in hexadecane) while the dispersed phase was an aqueous solution. A detailed study of the wettability properties of water and hexadecane was carried out in [15][16] by measuring their contact angles (CA), the results are reported in Fig. 1.7.

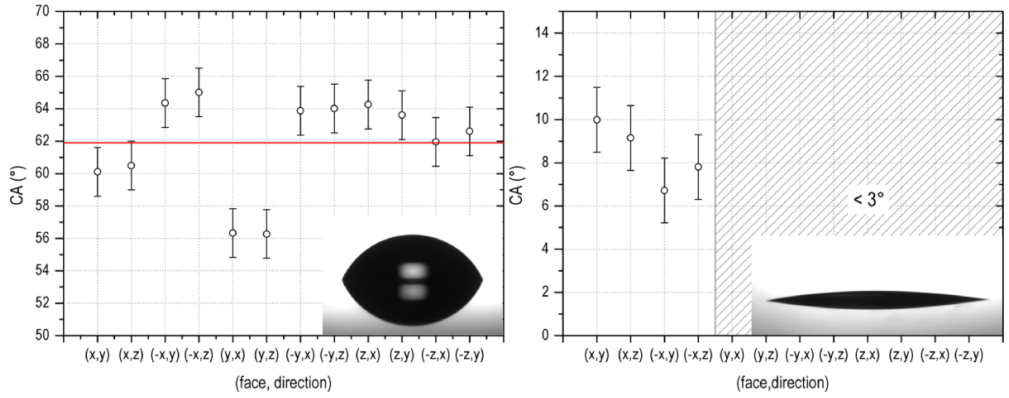

Figure 1.7: Contact angle (CA) measurements for different crystal cuts and crystallographic directions for: (a) water; (b) hexandecane.

Hexadecane completely wets the surface with a contact angle $CA < 10^o$ while water has an average CA of $(62 \pm 1)^o$, indicating a moderate hydrophobicity of lithium niobate.

In order to increase the contact angle of the water it was necessary to functionalize the channel. Consequently a solution of octadecyltrichlorosiolane (OTS) in toluene with a concentration of 100 μM was injected in the channels with a siringe pump. In figure1.8 are shown the measurements of the CA after the functionalization.

[2] $C_{24}H_{44}O_6$, CAS number:1338-43-8, Mm : 428.62 g/mol

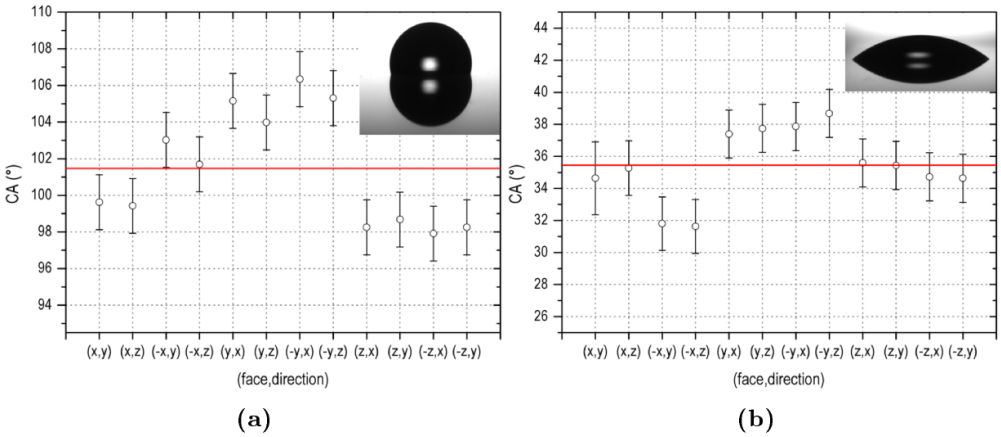

Figure 1.8: Contact angle (CA) measurements for different crystal cuts and crystallographic directions after functionalization for: (a) water; (b) hexandecane.

The contact angles of both the continuous phase and the dispersed one increased after the functionalization reaching a value of about $(101 \pm 1)^o$ for the water and $(35 \pm 1)^o$ for hexadecane.

In Fig.1.9 are shown pictures of the droplets inside the chip before and after the functionalization.

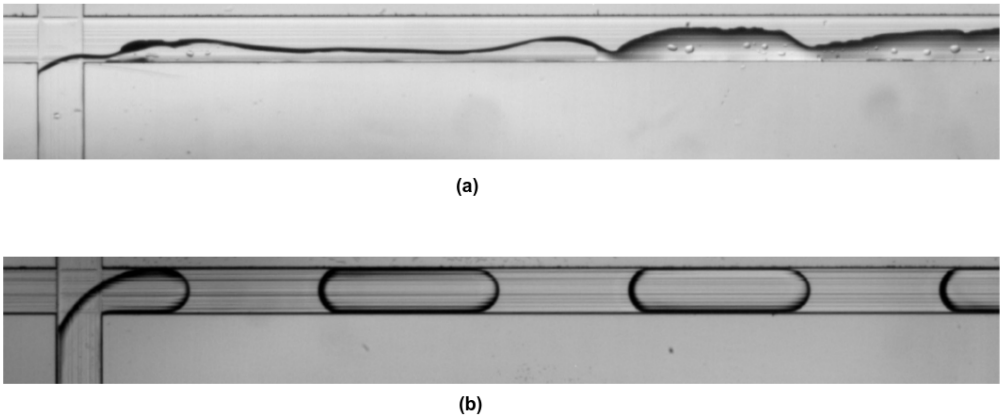

Figure 1.9: Contact angle (CA) measurements for different crystal cuts and crystallographic directions after functionalization for: (a) water; (b) hexandecane.

Chapter 2

Realization and characterization of planar waveguides in Lithium Niobate

Optical waveguides are defined regions where an electromagnetic wave can propagate and be confined by means of total reflection. Optical waveguides can be classified according to their geometry (planar, strip, or fiber waveguides), mode structure (single-mode, multi-mode), refractive index distribution (step or gradient index) and material (glass, polymer, semiconductor).

Waveguides are the first element of every integrated optical circuit and different techniques are available for their realization in lithium niobate, the most important are: titanium in-diffusion, proton exchange, ion implementation, laser writing. In this work of thesis the technique employed for the realization of the waveguides was titanium in-diffusion. The reasons for this choice were:

- the need for a high positive refractive index jump ($\Delta n > 0$) both in y- and z-propagating waveguides for the maximum versatility of the optofluidic device for future applications;

- the availability of all the facilities needed for the fabrication process (clean room, collimated UV lamp, magnetron sputtering, oven) at the Physics and Astronomy Department of Padova;

- the requirement to employ, for the realization of the device, techniques which are highly reproducible and easy to implement in order to facilitate the future technology transfer.

2.1 Waveguides realization

As mentioned in the previous section in this work of thesis the method used to realize optical waveguides was the titanium in diffusion. This technique and its diffusion profile depth can be controlled in a way that enables the creation of very thin waveguides able to support only the fundamental mode. This ensures that, if the beam coupled to the waveguide is gaussian, the fundamental mode will be gaussian at the exit and there will be no loss of information. Before describing in detail each step of the titanium in diffusion fabrication procedure the main steps are presented as guideline for the reader:

- photoresist layer deposition on the surface of the sample;
- thin stripes creation by keeping a mask in contact with the photoresist layer during the sample illumination with a UV lamp in order to impose degradation of the unmasked regions;
- titanium thin film deposition on the patterned surface by sputtering;
- removal of the photoresist layer by putting the sample in a solvent bath in order to leave on the crystal surface only the desired titanium stripes;

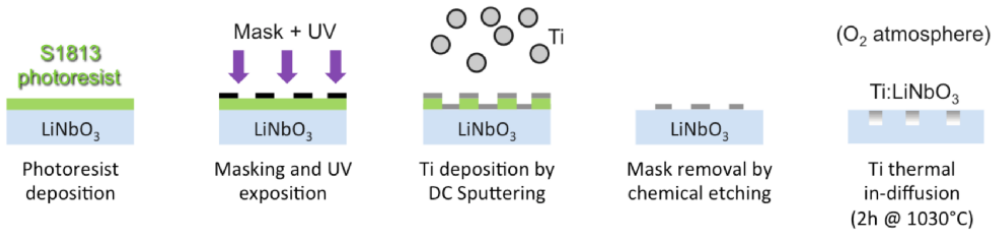

Figure 2.1: In this picture the main steps of the titanium in diffusion fabrication process are shown.

In the following the waveguides realization steps will be presented in detail.

Samples cutting At first the samples were cut with the desired dimensions from a commercial x-cut wafer of congruent lithium niobate[1]. The cuts were performed with a South Bay 540 cutting machine, equipped with a diamond-coated Cu-alloy blade. Each sample underwent a sonicating bath in soap and distilled water, isopropanol and finally acetone for 15 minutes respectively to ensure a clean surface before the sputtering deposition.

Photolitography All the photolitography steps were performed in a ISO 7 class clean-room financed by the MISCHA project (Microfluidics laboratory for scientific and technological applications). The photoresist employed was the S1813 from the Microposit S1800 G2 series. It is a positive photoresist engineered to satisfy in particular micro-litography on silicon but it showed to be suitable also on lithium niobate. It was chosen for its compatibility with the emission spectrum of the available UV lamp and for its nominal resolution of 0.48 μm, suitable for our purpose. At first the samples were covered with a primer based on hexamethyldisilizane (HMDS) to favour the adhesion of the phtoresist to oxides. Both the primer and the photoresist were deposited by spin coating at a spin rate of 2000 rpm for 30 s and 6000 rpm for 30 s respectively. A mask with patterns of stripes with different widths (3, 5, 6, 8, 10 μm) was realized by a specialized company (Delta Mask B.V.). It consisted in a laser patterned chromium layer of 980 Å on a plate of Soda Lime glass. After the photoresist deposition the samples were put under the mask, in deep contact with it and exposed to UV irradiation from a highly collimated UV lamp with an intensity of 9mW/cm 2 for 18s. The photoresist was then developed by dipping in a stirred bath of Microposit MF-300 for 60s and then rinsed in a distilled water bath. The quality and the width of the obtained channels were controlled by optical microscopy and profilometry.

Titanium deposition. Sputtering deposition consists in the deposition of atoms which are removed from a metallic or insulating target after bombardment by the ions of a plasma on the sample surface. The process takes place in a vacuum chamber at a controlled pressure and the plasma is sustained by a potential difference between the target and the rest of the chamber. Alternating current source, which is mandatory for the sputtering of insulating materials. In the magnetron sputtering a magnetic field is also present in

[1]Crystal Technology with a thickness of 1mm and polished on both faces.

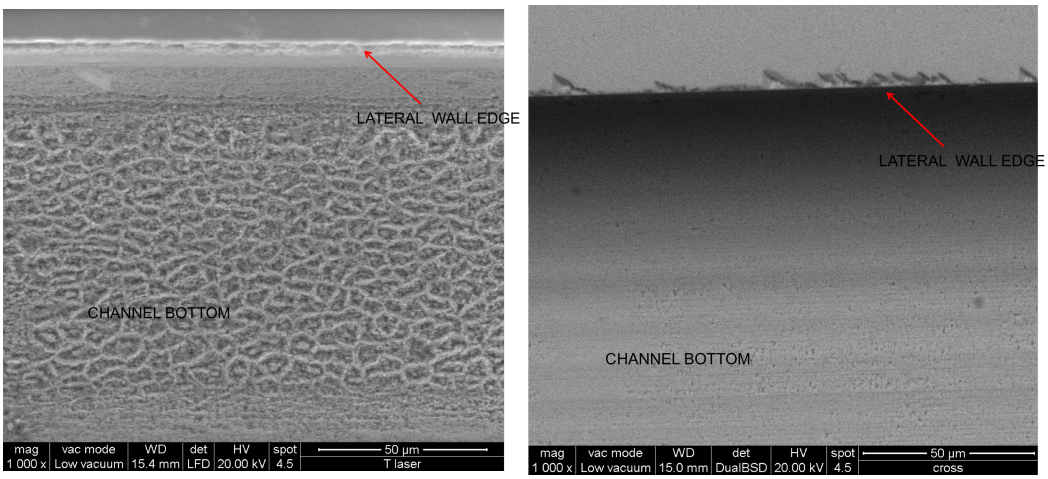

Figure 2.2: Image on th left: SEM image of the T-junction; **Image on the right:**SEM image of a cross junction.

the proximity of the target due to permanent magnets. These magnets have the aim to confine secondary electrons coming from the collisions between the plasma ions and the target in order to increase the cationic density in the region of the target and allow for a higher sputtering rate. The deposition of the titanium film was performed by a magnetron sputtering machine provided by Thin Film Technology. The samples were kept in a cylindrical vacuum chamber at a pressure below $3 \cdot 10^{-6}$ $mbar$, achievable with two subsequent stages: a rotary vacuum pump was used to reach a pressure of $(8 \div 9) \cdot 10^{-2}$ $mbar$ and a turbomolecular pump allowed reaching the minimum pressure. Argon gas was injected in the chamber through a flow-meter at a pressure of $5 \cdot 10^{-3}$ $mbar$ to feed the plasma. The titanium target was connected to a DC power source supplying a power of 40 W during the deposition. The target was kept covered by a shield during a pre-sputtering time of 3 minutes in order to remove impurities and oxidized layers on its surface. Normal operation required to put the samples on a sample holder laying at the center of the cylindrical chamber and tilt in their direction the target holder which was positioned out-of-axis. In this way sputtered titanium atoms reached the samples at a certain angle and this feature was found to be detrimental during the lift-off process when channel waveguides have to be realized. Actually this configuration led titanium atoms to impinge on the lateral walls of the channels realized in the photoresist rather than on their bottom. A dedicated sample holder was then designed in order to keep the samples in front of the target and ensure titanium atoms trajectories to

be perpendicular to the sample surface. The typical thickness of the final film is of the order of magnitude of a few microns.

Lift-off. The photoresist and the titanium deposited on its surface were removed by a bath in the SVC(TM)-14 specific stripper at 60 ^oC for several minutes and then under sonication for few seconds.

Thermal diffusion. The diffusion process was performed in a tubular furnace Hochtemperaturofen Gmbh (model F-VS 100-500/13) by Gero. The sample was positioned on a platinum foil laid on the boat at the end of a quartz rod used to pull them at the center of the oven. The channel waveguides were diffused at a temperature of 1030 ^oC for 2h. The heating and cooling rates were always kept to 300 ^oC and 400 ^oC respectively to avoid excessive thermal stresses of the crystals. Oxygen was fluxed inside the oven chamber at a flow rate of 50 Nl/h to reduce surface damage after titanium in-diffusion. Unfortunately wet conditions were not possible with the available set-up so that the optimal conditions reported in literature to avoid lithium out-diffusion were not reached.

Lapping and polishing. At the end of the process all samples lateral surfaces were lapped and polished to remove the damages and defects caused by the cutting from the original commercial wafer. The process was carried out with a professional polishing machine by Logitech. The polishing is performed by making the samples laying on a rotating disk. The procedure requires three subsequent steps employing an iron disk wet by an aqueous suspension of 9 μm alumina particles, the same disk wet by an aqueous suspension of 3 μm alumina particles and finally a polyurethane disk wet by an aqueous suspension of submicrometer particles. At the end of the procedure a surface roughness of the order of 1 nm is obtained.

2.1.1 Titanium in-diffusion

Titanium in-diffusion process was studied in detail in the past and the process was found to go through the following steps:

- $T \sim 500^oC$: titanium is oxidized to TiO_2 ;
- $T > 600^oC$: $LiNb_3O_8$ epitaxial crystallites are formed at the surface together with the simultaneous loss of lithium;
- $T > 950^oC$: a $(Ti_{0.65}\ Nb_{0.35}\ )O_2$ mixed oxide source appears and it acts as the diffusion source for titanium in-diffusion inside the bulk crystal.

In general metal diffusion inside oxides from a thin metallic layer is described starting with the well-known Fick's law:

$$\frac{\partial C(x,t)}{\partial t} = \frac{\partial}{\partial x}\left(D\frac{\partial C(x,t)}{\partial x}\right) \tag{2.1}$$

where $C(x,t)$ is the dopant concentration and the diffusion coefficient D can be dependent on both the temperature T and the concentration C(x,t). The dependence of D on the temperature is usually modeled by an exponential law according to Arrenhius theory: $D = D_0 e^{-E_a/k_B T}$, where E_a is the activation energy. If the film is not completely diffused it can be approximated as an infinite source of dopant because at the surface of the crystal the concentration is constant and equal to the saturation concentration C_s . The solution is described by an error function:

$$C(x,t) = C_s erfc\frac{x}{\sqrt{4Dt}} \tag{2.2}$$

In the case of a diffusion time much larger than the time needed to exhaust the film, the approximation of the dopant source at $t = 0$ as a layer with negligible width can be made ($C(x, t = 0) = 0$ only for $x = 0$) and the solution to the Fick's equation has a Gaussian shape:

$$C(x,t) = \frac{M}{\sqrt{\pi Dt}} e^{-x^2/4Dt} = C_0 e^{-x^2/4Dt} \tag{2.3}$$

where M is the total amount of dopant deposited in the film and $C_0 \sim \sqrt{t}$ is the concentration at the surface of the crystal at time t. In the case of a titanium in-diffused planar waveguide the general condition to be achieved is that of a completely diffused dopant so that a simple Gaussian can be used to fit the diffusion profile along the surface orthogonal direction.

In particular the waveguides were fabricated in order to couple them with a 632.8 nm wavelength Gaussian beam in a single mode configuration.

2.2 Waveguides characterization

A near field experimental set-up was built in order to couple the waveguide to a laser source and measure the near field image of the mode sustained and its output intensity. This means that the spatial distribution of the intensity transmitted by the waveguide is recorded and can be analyzed.For these measurements a laser beam was focused on the head of the waveguide and the trasmitted light is collected by an objective lens and recorded by a digital camera. The set-up used for the near field characterization of the waveguide, shown in Fig.2.3, includes:

- A He-Ne laser at a wavelength of 632.8 nm with a nominal power of 4 mW;
- an half-wave plate and a polarizer to turn to select the polarization in order to excite the TE or TM mode of the waveguide;
- two confocal lenses used to increase the laser beam width from 1 mm to 4 mm (width of the entrance pupil of the objective).
- a 20× obective to focus the laser beam before coupling to the waveguide;
- a three dimensional translational and rotational stage to move the sample allowing the alignment with respect to the input beam;
- an horizontal microscope with a 20× objective with a working distance of 1.2 cm and two different zoom levels, moved by a three-dimensional translational and rotational stage;
- A LaserCam-HR camera by Coherent Inc. to record the near field image.

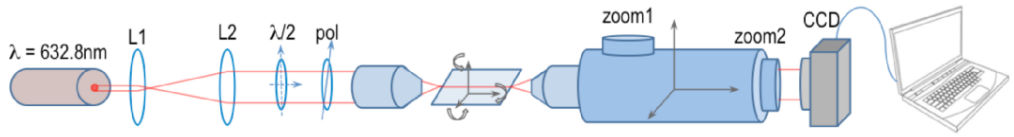

Figure 2.3: Sketch of the optical line used for the near field characterization of the waveguides.

The reference framework is fixed so that the axes are oriented in the same directions as the crystallographic directions of the sample with the z-propagating waveguides aligned along the laser beam.

The entire procedure of the near field analysis comprehends the study of the spatial distribution of the intesity of the transmitted beam.[15] The images of the transmitted beam were recorded and the waveguide alignment was carried out optimizing the light intensity and symmetric spatial distribution. In particular in this work of thesis six x-cut samples have been analyzed for a total number of seventy waveguides (the mask used was such that the sample was supposed to have twenty waveguides). For each guide two images were recorded: one for the TE mode and one for the TM mode. In Figure2.4 an example of an image of a waveguide, obtained with the set-up described above, is shown.

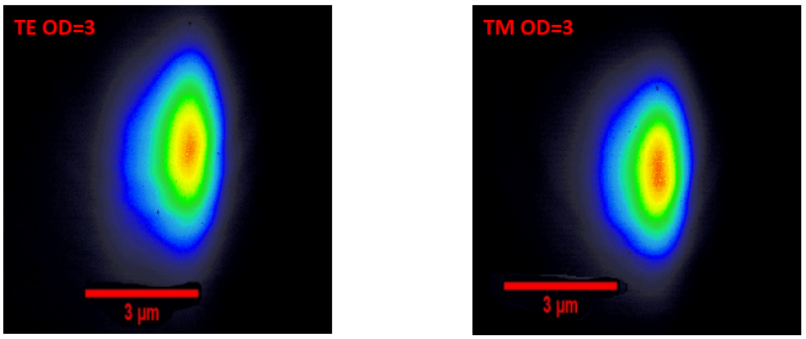

Figure 2.4: Example of the images of a waveguide in TE and TM mode.

When many optical guides are realized on the same substrate, it is mandatory to define a way to compare their performance and to test the reproducibility of the preparation process. The symmetry of the waveguides is important especially as it is a necessary requirement to couple the chip with an optic fiber (is important for future LOC applications). In order to do so the images have been analyzed by an ad hoc software which allows to study the waveguides' symmetry along four different directions: the x-axis perpendicular to the surface of the sample, the y-axis parallel to the surface and the two diagonals as shown in Fig.2.5

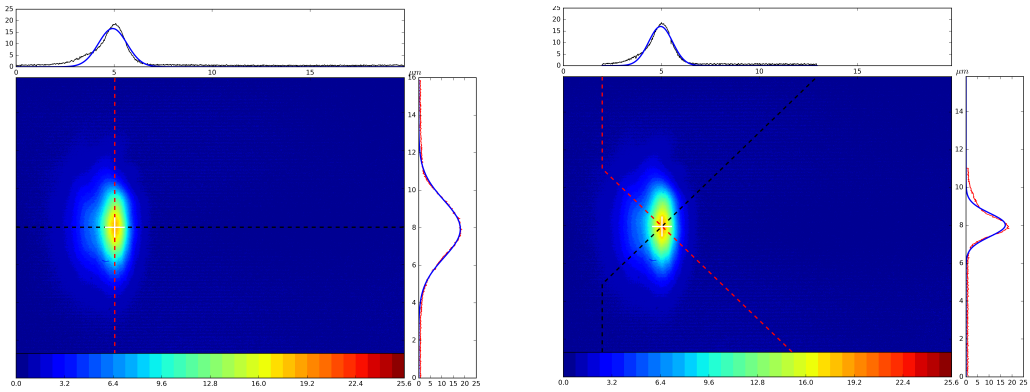

Figure 2.5: Example of the output of the program used for the waveguides' analysis. The red and black curves are the intensity profiles of the guides, the same colours are used to indicate the corrisponding directions. The blue curve represents a gaussian fit.

The images recorded with the CCD are ASCII images which can be reguarded as matrices of pixels whose values are proportional to the intensity of the signal in that point.
As first step, the program, calulates the position of the centroid of the waveguide, by placing it in a region around the maximum intensity value. It then removes the background which is calculated as mean value of the marginal areas intensities. Once the centroid and the background have been calculated the program calculates the intensity curves along the different directions and the integrals of the curve's tails from a value of zero intensity up to the 16% of the maximum. The starting point of the program for the calclus of the intensity curves is the centroid of the waveguide. The physical parameter that was implemented in order to estimate the degree of the optical mode symmetry is P, i.e. the difference between the two integrals normalized to their sum:

$$P_{X,Y} = \frac{I_{left} - I_{right}}{I_{left} + I_{right}} \tag{2.4}$$

This parameter is the mean value of intensity along the x and y directions. As for the mean value along the diagonals, the diagonal's ratio DR is calculated using:

$$DR = \frac{(I_{1,left} - I_{1,right})/((I_{1,right} + I_{1,left})}{(I_{2,left} - I_{2,right})/((I_{2,right} + I_{2,left})} \tag{2.5}$$

where $1, 2$ are the two diagonals of the same image, and I are the integrals calculated in the range of zero intensity up to the 16% of the centroid intensity. The two parameters, calculated averaging over all the images are [16] :

Mode	Mean x-axis	Mean y-axis	DR
TE	0.23±0.02	0.038 ± 0.006	1.00 ± 0.07
TM	0.26±0.02	0.059 ± 0.006	0.96 ± 0.05

Table 2.1: Values obtained from the study of the waveguides symmetry.

Table 2.1 can be used to demonstrate the waveguides high symmetry: the near-zero mean value along the y direction and the diagonal's ratio mean value of one are proof of this. The x direction shows a mean value much higher than the y direction due to the fact that along this axis we have to consider both air and lithium niobate, which have different refractive indices, as the waveguide is in between these mediums.

No significant differences were observed comparing the TE and the TM modes.
Given the high number of waveguides analyzed this study has proven to be very reliable over the analysis of the waveguides' symmetry.
This study has proven the validity of the Titanium-in-diffusion technique for the realization of planar waveguides in Lithium Niobate and the possiblity to couple with optic fiber.

Chapter 3

Microfluidics Characterization and Optofluidic Coupling

The study of the droplets flowing inside the microfluidic channels was performed controlling the flow rates injected in the microfluidc chip and exploiting a fast imaging system, based on the recording of image sequences with a fast camera connected to a microscope.

3.1 Experimental apparatus

The microfluidic device, presented in the previous chapter, was used in the cross-flowing configuration as a droplet generator.
The injected fluids were hexadecane[1] as continuous phase and distilled water as dispersed phase. The surfactant (SPAN®80), was added to the continuous phase to reduce the interfacial tension σ between the two fluids.
The microfluidic set-up used for the measurements (shown in Fig.3.1) is composed by an ELVENFLOW OBI Mk3 pressure driven pump coupled with two Coriolis-based flow sensors (BRONKHORST), that were employed to inject the fluids and control their fluxes (my means of an apposite software ELVENFLOW provided by the same company) inside the microfluidic channels of the chip. The flow sensors are connected to the chip through flexible polyethylene tubings by Deutsche & Neumann (ID=0.5 mm, OD=1.0 mm, resistant to acids, bases, alchools and salt solutions up to 80^oC) which were inserted in the larger Masterflex®silicone tubing ($OD = 4\ mm$; $ID = 0.8\ mm$).
As the fluids flow inside the chip, the light output is measured.
The collecting objective employed in the near field setup was chosen with a

[1]Hexadecane:$CH_3(CH_2)_{14}CH_3$, CASnumber: 544-76-3, $Mn = 226.44\ g/mol$, viscosity 3 cP, density at 20^oC 0.77 g/cm^3

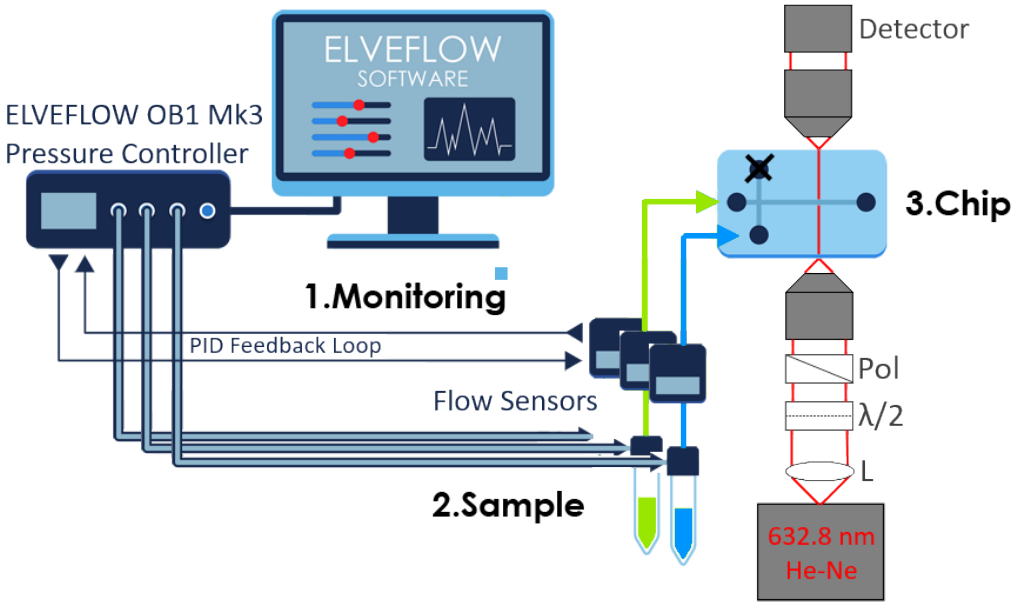

Figure 3.1: Sketch of the set-up used in ths experiment.

working distance of 1 cm. The key parameter to be studied in this opto-fluidic system is the light transmitted across the microfluidic channel.
Since in this case there is no more interest on the shape of the mode of the waveguide but the aim is to measure the overall intensity exiting from the output waveguide, a simple photodiode was used in place of the CCD fast camera used in the near field characterization. A transimpedence was put in series to the photodiode in order to convert and amplify the signal into a voltage which was monitored with an Agilent MSO-X 2012A oscilloscope.

This transimpedence allowed to amplify the collected signal by a factor of 10^7. The signal was than recorded using a Analog to Digital Fast Card NI 6023E. This card can guarantee a measurement sensitivity of voltage reading of 0.0023 mV and a maximum sample rate of 200 KS/s and is controlled by a LabView program. The images of the droplets were acquired simultaniously by means of a fast camera Basler acA800-510um.

3.1.1 Data Acquisition

The channels were filled with hexadecane ($n_{hexad} = 1.434$ at $\lambda = 632.8\ nm$) to allow for a better index matching between the lithium niobate crystal and

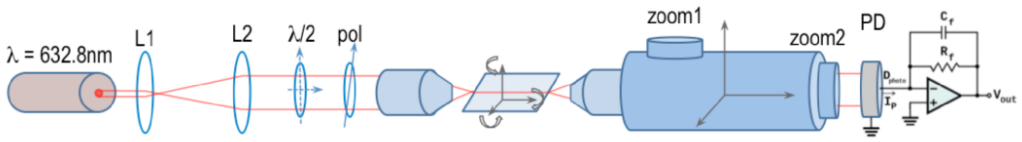

Figure 3.2: Sketch of the experimental system used to perform time resolved measurements of the transmitted intensity exiting from the collecting waveguide while fluids are flowing.

the fluid inside the channel. The first step consisted in using a chopper to produce a square wave signal which was detected by the oscilloscope and allowed the adjustment of the position of the chip in order to record the highest signal possible.
Once the chip was set in the right position the water was inserted in the chip and the output signal was reported as a function of time, thanks to a dedicated LabView program.

The signal from the TE single-mode of a z-propagating waveguide was registered during the passage of the generated droplets. When a train of droplets is generated, the voltage signal recorded has the shape of a square wave, where the higher plateau refers to the flow of the continuous phase while each lower plateau indicates the passage of a water droplet (see Fig.3.3). Both

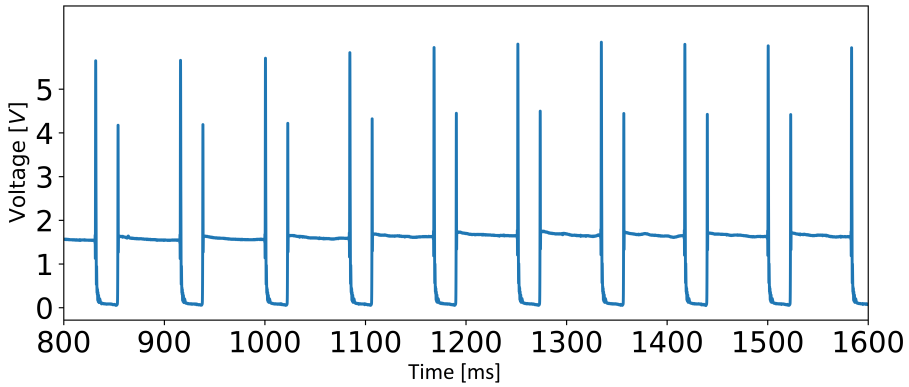

Figure 3.3: Acquisition profile of ten droples.

the rise and the fall of the square wave are characterized by a sharp peak in proximity of the higher plateau. These peaks correspond to the passage of the advancing and the receding menisci of the droplet(see Fig.3.4).

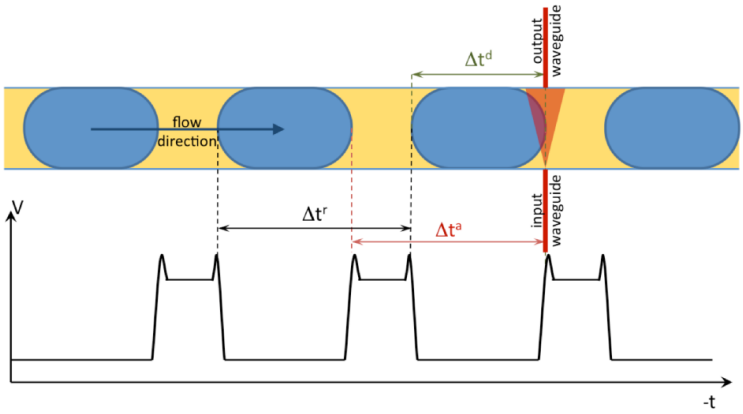

Figure 3.4: Sketch of the droplets passages and relative detection ($n_{droplet} > n_c$).

3.1.2 Data analysis

In this work of thesis a given protocol has been developed: for each acquisition the fluids' flux was controlled and both a voltage signal and microscope images of the droplets were recorded.

In particular, the flux of the dispersed phase Q_d was fixed while varying the values of the flux of the continuous phase Q_c, obtaining flow rates in the range of $\phi = \frac{Q_d}{Q_c} \sim 0.05 \div 1$.
It is important to mention that, this protocol is different from conventional microfluidic experiments, in which the flux of the continuous phase is generally kept constant while varying the dispersed phase flux. The reason for this approach is dictated by the fact that the aim of this work of thesis is to create a LOC device for possible biological applications; in order to work with biological samples which are very delicate, it is generally safer to keep the flux of dispersed phase containing the sample fixed while varying the flux of the continuous phase.
In particular, two different approaches have been studied in this work of thesis:

- **Varying the flux of the dispersed phase Q_d:** For every acquisition the fluxes of the continuous and dispersed phase were controlled, fixing the value of Q_d and varying the values of Q_c. The values of the fluxes of the dispersed phase analyzed in this work of thesis are $Q_d = 5, 10, 15, 20, 25\ \mu l/min$.

- **Varying the density of the dispersed phase keeping Q_d fixed:** different solutions of glycerol-in-water have been prepared verying the glycerol concentration: 0 %, 10%, 25% and 50% solutions have been

studied. For every acquisition the dispersed phase flux was kept at a fixed value of $Q_d = 20\ \mu l/min$ while varying the values of Q_c.

The experiments were conducted in a wide range of flow rates ϕ covering both the squeezing and an intermediate squeezing-to-dripping regime. The analysis of both the optical signal and the collected images allowed the distinction of the two regimes as it will be described in the following sections and in Chapter 4.

Voltage signal analysis

The typical signal acquired is reported in Fig.3.5.

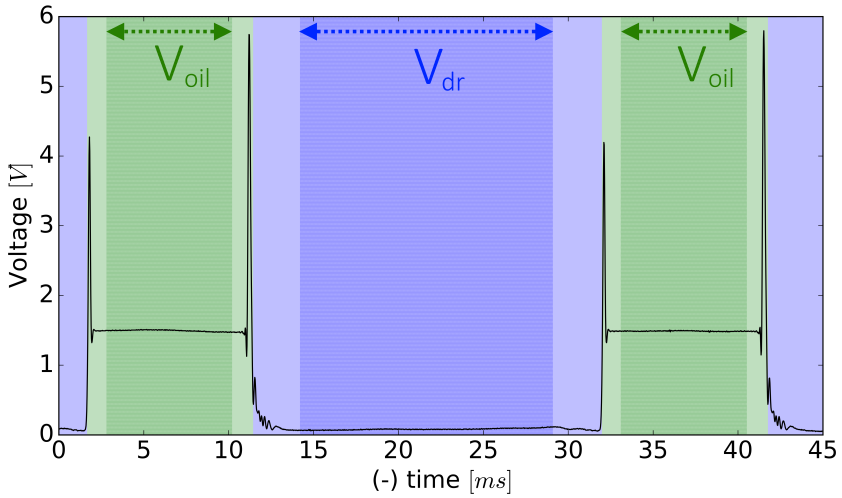

Figure 3.5: Example of the signal obtained. Where the oil and water plateaux are highlighted.

As mentioned in the previous section, when a train of droplets is generated, the voltage signal recorded has the shape of a square wave where the higher plateau refers to the flow of the continuous phase while each lower plateau indicates the passage of a water droplet. The sharp peaks in proximity of the higher plateau are called primary peaks and correspond to the passage of the advancing and the receding menisci of the droplet (see Fig.3.4).

The optical signal of each droplet is then analyzed with a specific software written in Python.

For each drop the program calculates:

- the **integral** I of the curve, intended as the area under the acquisition profile from the first peak to the second one (as shown in blue in Fig.**??**(a)). It is calculated as:

$$I = \frac{\int_{t_{start}}^{t_{end}} V_{droplet}}{\bar{V}_{hexa} \cdot [t_{end} - t_{start}]} \tag{3.1}$$

  Where $\bar{V}_{hexa}$ is the mean voltage corresponding to the hexadecane.

- the **minimum** V_{min} value of the signal;

- the **length** $L(ms)$ of the drop expressed in ms, calculated as the temporal difference between the minima neighbouring (the green points in Fig. **??**) the sharp peaks of each droplet and considering the mean value as the actual length of the droplet;

- the **left integral** I_{left}, calculated as the area under the curve from t_{start} to the minimum value of the curve expressed in terms of time t_{min} normalized over the value of the hexadecane plateau:

$$I_{left} = \frac{\int_{t_{start}}^{t_{min}} V_{droplet}}{\bar{V}_{hexa} \cdot [t_{min} - t_{start}]}; \tag{3.2}$$

- the **right integral** I_{right}, calculated in the same manner as I_{left}, in the interval $[t_{min}; t_{end}]$:

$$I_{right} = \frac{\int_{t_{min}}^{t_{end}} V_{droplet}}{\bar{V}_{hexa} \cdot [t_{end} - t_{min}]}; \tag{3.3}$$

The main objective of this work of thesis is to correlate optical parameters with physical properties of the droplets with the perspective to develop LOC devices.
In fact the integral of the signal is related to the curvature of the droplet as it measures the intensity of the transmitted light (lens effect).
The minimum of the signal is a fingerprint of the trasmittivity. When the droplet is in the squeezing regime, the plugs touch the channels and the resulting signal presents a plateau. As the transition squeezing-to-dripping begins the droplets acquire a more spherical shape and the minimum corresponds to the point where the droplets touch the walls of the channel (see Fig.**??**)

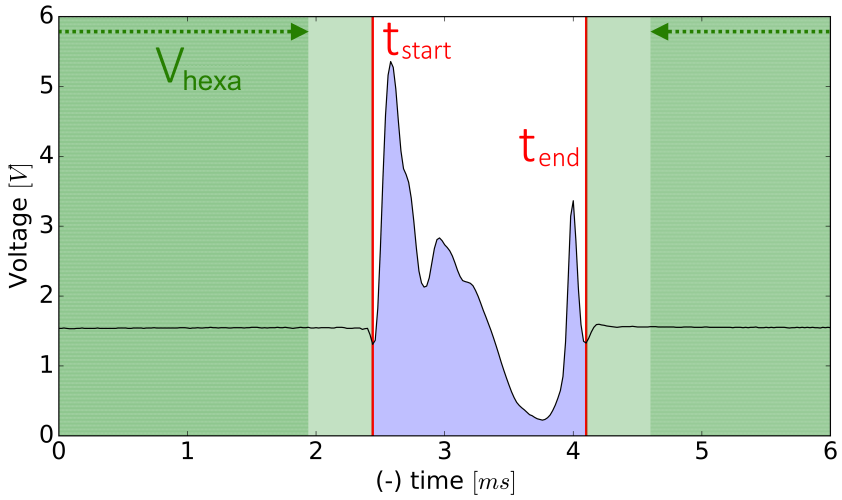

Figure 3.6: Right and left integrals of the acquisition profile.

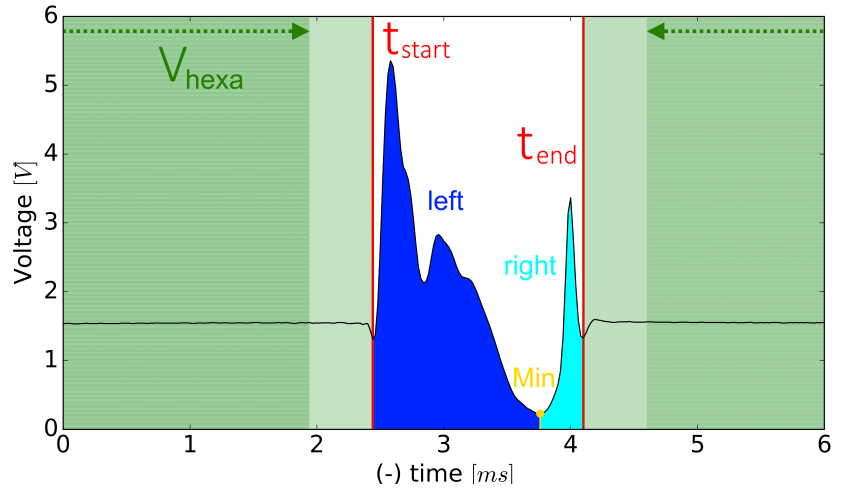

Figure 3.7: Integral of the acquisition profile.

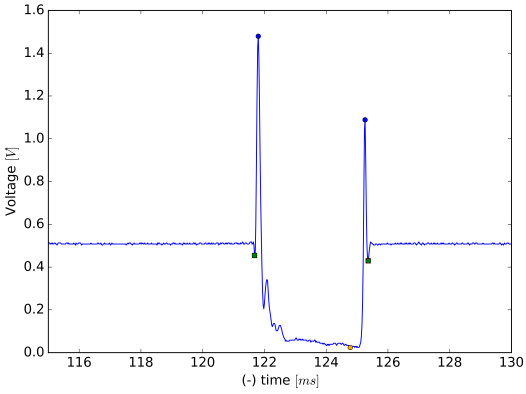

Figure 3.8: Acquisition profile. The green points are the minimum points used to compute the length parameter (time the droplet takes to pass in front of the waveguide).

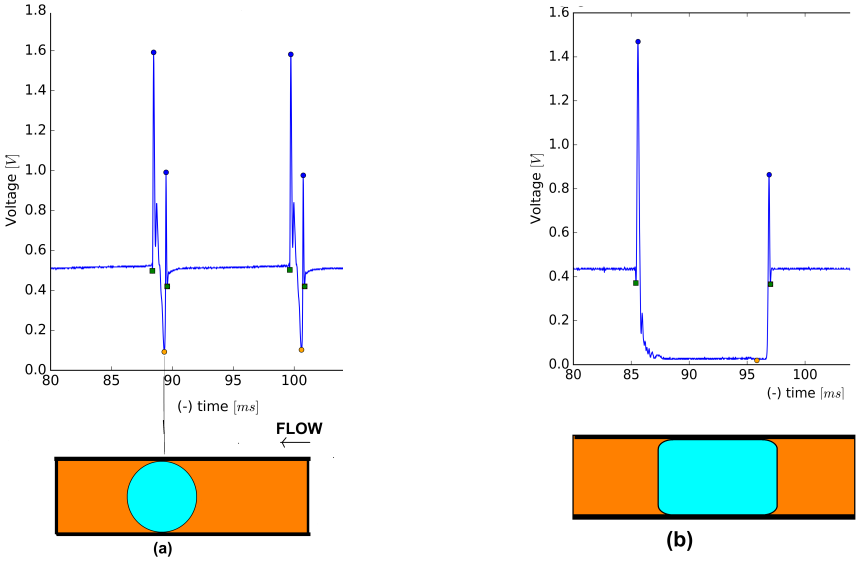

Figure 3.9: **a:** Dripping Regime; **b:** Squeezing Regime.

Image sequence analysis

A fast camera Basler acA800-510um with a plan $10 \times /0.10$ objective with a 10 mm working distance, placed under the sample (see Fig.3.10), was used to record the image sequences. The analysis of the images was performed with the aid of an ad-hoc software developed by Enrico Chiarello, in the framework of the LaFSI group at the Department of Physics of the University of Padova.The software is based on the analysis of the contrast of the images and is able to recognize the droplets flowing in the channel calculating their length, speed and passage time respectively. The length of a droplet is determined from each single and the average length of the droplet in the considered flux regime is then calculated.

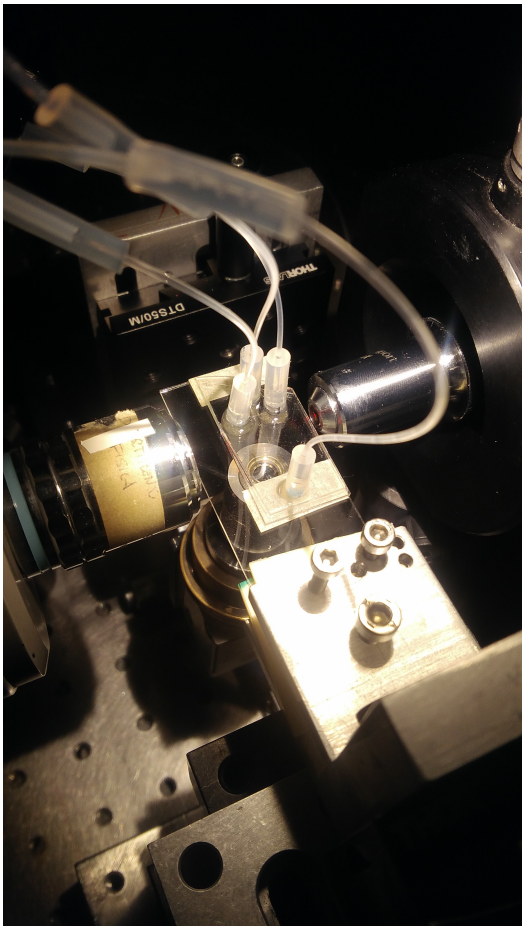

Figure 3.10: Picture of the sample. The camera Basler acA800-510um is placed under the sample.

Chapter 4

Results

In this chapter the results of the data analysis will be discussed.

The main objective of this work of thesis is to relate optical parameters to microfluidic parameters with the prospective to elaborate a suitable LOC device. Droplets with different shapes, as discussed in the previous chapter, are related to signals which are characterized by a complex dynamic trend but with typical fingerprints.
The analysis of the trasmittivity of the signal of a droplet which flows inside a microfluidic channel is not easy to describe as it is influenced by refraction and diffraction phenomena.
It is therefore mandatory to study, at least with a phenomelogical approach, the shape of the signal and to associate it to some reliable parameters. In particular it is necessary for the parameters to be reproducible and to contain informations coherent with the physical characteristics of the droplet itself. In order to do so, different optical parameters, deriving directly from the voltage signal recorded by the CCD, have been studied as a function of the flow rate $\phi = Q_c/Q_d$ in two cofigurations:

- Changing the shape of the droplet by varying the dispersed phase flux $Q_d = (5, 10, 15, 20, 25)\mu l/min$ for each acquisition, consequently ;
- Changing the viscosity by keeping fixed the value of the dispersed phase flux $Q_d = 20\ \mu l/min$ and varying the concentration C of glycerol of the solution prepared as dispersed phase. The solutions used had $C = 0\%, 10\%, 25\%, 50\%$.

The study of the droplets behaviour in a wide range of Q_c gives informations over the geometry of the droplet. In particular a feature of interest is the identification of the droplet production regime. The experiments were performed in a wide range of flow rates covering both the squeezing and an

intermediate squeezing-to-dripping regime (the definition of squeezing and dripping regimes can be found in chapter 3). In fact, considered the dripping regime as the regime in which the droplet is spherical and is not influenced by the geometry of the apparatus, this regime is never reached in this experiment.

The data analysis allowed to find a value ϕ^* of the flow rate for each flux Q_d which can be interpreted as the beginning of the transition from squeezing to dripping regimes. As mentioned in the previous chapter the software used to analyze the optical signal of the droplets returns: the length of the droplet expressed in ms, the minimum value of the signal, the integral of the droplet, and the left and right integrals.

In the following the various parameters will be discussed in detail.

4.1 Droplets Length

The first parameter to be analyzed is the length of the droplet. The parameter obtained from the optical analysis is actually a value proportional to the time taken by the droplet to pass in front of the waveguide, computing the distance between the two minima in correspondence of the primary peaks of each droplet (as described in the previous chapter).
This parameter therefore returns a length expressed in ms. In the following the length of the droplet is shown as a function of the flow rate for different values of the dispersed phase flux $Q_d = 5, 10, 15, 20, 25\ \mu l/min$ Fig.4.1 and for a fixed value of $Q_d = 20\ \mu l/min$ with different concentrations of glycerol C (see Fig.4.2-**??**), where the red lines represent the linear fit of the experimental data.

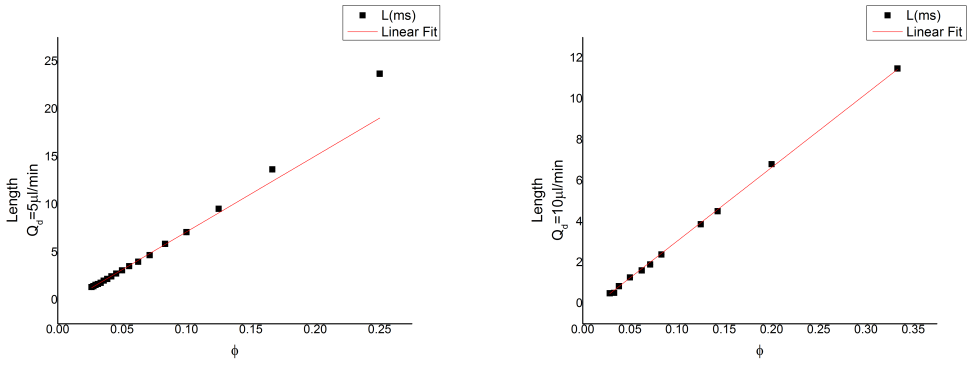

Figure 4.1: Droplets' Length in ms for $Q_d = 5\ \mu l/min$ (left) and $Q_d = 10\ \mu l/min$.

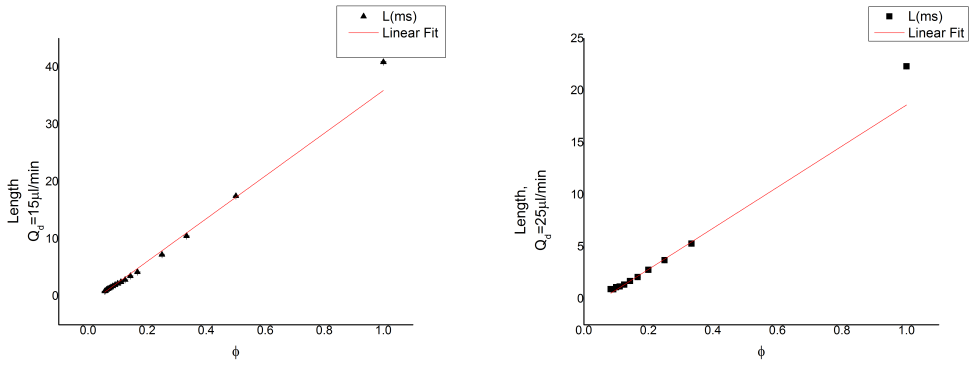

Figure 4.2: Droplets' Length in ms for $Q_d = 15\ \mu l/min$ (left) and $Q_d = 25\ \mu l/min$.

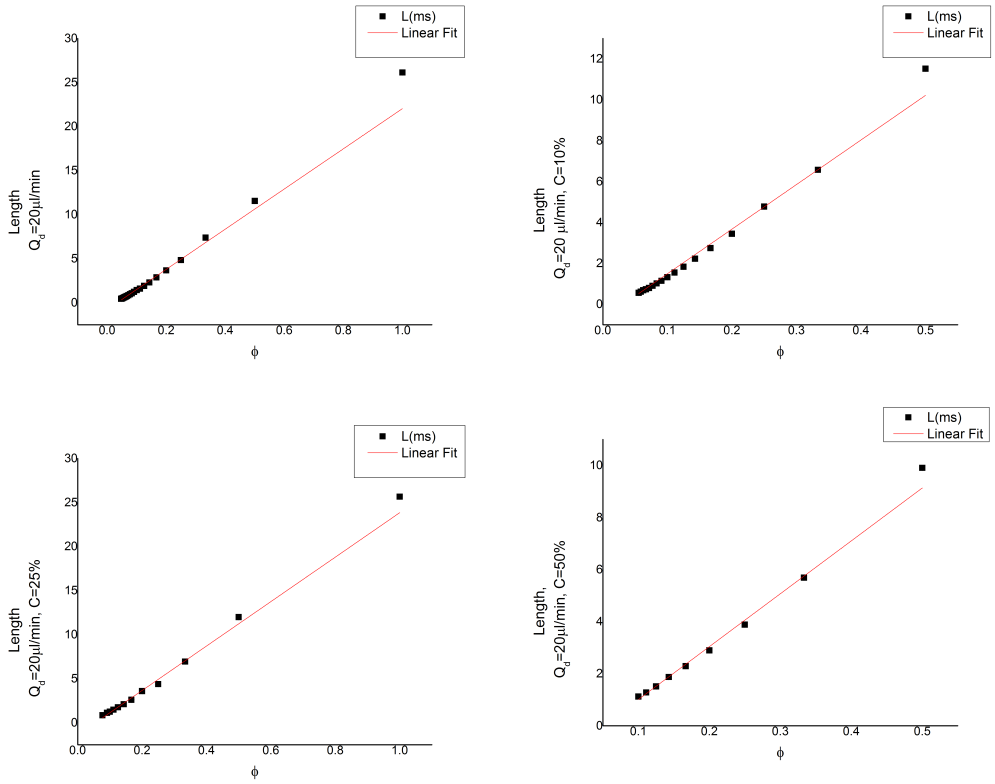

Figure 4.3: Droplets' Length in ms for $Q_d = 20\ \mu l/min$ and $C = 0\%$ (top left), $C = 10\%$ (top right), $C = 25\%$ (bottom left) and $C = 50\%$(bottom right).

In literature the most stressed scaling relation describing the T-junction is the linear dependence of the droplet length on the flow rates ratio ϕ. As shown in the plots above, the length of the droplet L on the flow rate ϕ follows the linear dependence expected with no large deviations from this trend exept for the points at higher flow rates.
In table4.1 the parameters of the linear fit $y = m \cdot x + q$ are reported.

Q_d $[\mu l/min]$	**m**	**q**
5	79.5 ± 1.9	-0.82 ± 0.07
10	36.0 ± 0.4	-0.56 ± 0.03
15	37.3 ± 0.8	-1.4 ± 0.1
20	22.8 ± 0.6	-0.77 ± 0.06
$20 glycerol 10\%$	20.8 ± 0.2	-0.62 ± 0.03
$20 glycerol 25\%$	25.2 ± 0.9	-1.4 ± 0.1
$20 glycerol 50\%$	20.3 ± 0.7	-1.0 ± 0.1
25	19.7 ± 0.8	-1.1 ± 0.2

Table 4.1: Values of the linear fit of the droplet length as a function of flow rates ratio ϕ for $Q_d = 5, 10, 15, 20, 25$ $\mu l/min$.

The length of the droplet can also be obtained by means of the images recorded with the camera, through an ad-hoc software.
Fig. 4.4 shows the values of the rescaled length $\bar{L} = \frac{L}{w}$ as a function of the flow rate ϕ.

The trend followed by the graphs is clearly not a linear one. The experimental data exhibits a power trend, instead. The values obtained from the interpolation with the function $\bar{L} = a \cdot \phi^b + c$ are reported in table4.2.

Given the time of passage in front of the waveguide $L(ms)$ and the rescaled length of the droplet it is possible to calculate the velocity of the droplet. In particular, larger drops are slower and allow to measure the velocity in a more accurate way than smaller droplets which are faster and harder to measure with set-up used in our experiment.

As a measure of the velocity of the droplets would only be accurate for high flow rates this parameter was not calculated in this work of thesis. It

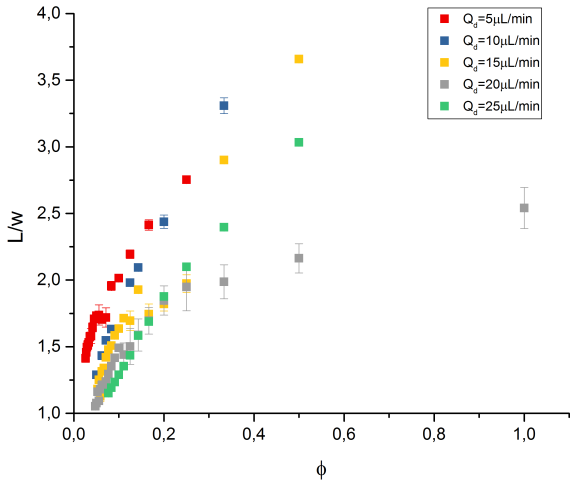

Figure 4.4: Droplets' rescaled lengths $\bar{L}$ as a function of flow rates ratio ϕ.

Q_d $[\mu l/min]$	**a**	**b**	**c**
5	0.4 ± 0.2	-0.5 ± 0.6	4.0 ± 0.6
10	$1 \pm 2*$	$2 \pm 2*$	$3 \pm 3*$
15	0.42 ± 0.05	0.12 ± 0.14	3.5 ± 0.1
20	0.29 ± 0.02	0.19 ± 0.04	3.64 ± 0.07
$20 glycerol 10\%$	0.74 ± 0.07	-0.24 ± 0.08	2.46 ± 0.09
$20 glycerol 25\%$	0.89 ± 0.05	-0.14 ± 0.09	2.18 ± 0.04
$20 glycerol 50\%$	0.28 ± 0.05	0.3 ± 0.2	4.1 ± 0.2
25	0.49 ± 0.04	0.039 ± 0.07	2.71 ± 0.07

Table 4.2: Values of the linear fit of the droplet length as a function of flow rates ratio ϕ for $Q_d = 5, 10, 15, 20, 25$ $\mu l/min$. Values marked with * are only qualitative.

is interesting to notice however, how Fig.4.5 shows, that while slow droplets are strongly dependent on the dispersed phase flux, smaller droplets tend to the same velocity.

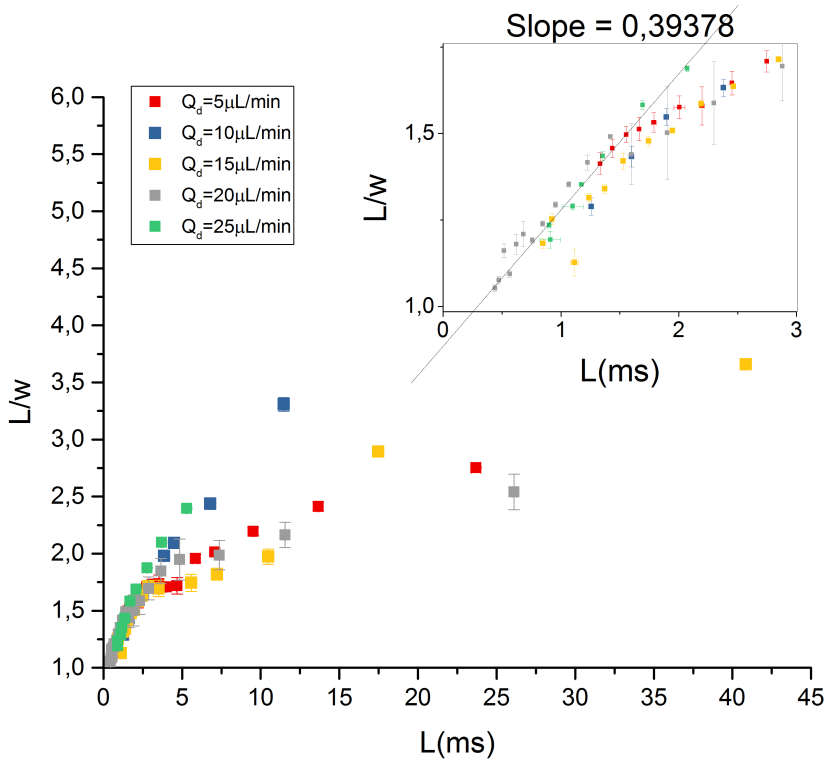

Figure 4.5: Droplets' rescaled length as a function of the droples' duration($\propto L$).

4.2 Minimum of the signal

The minimum of the signal is usually a parameter of interest as it gives informations over the trasmittivity of the signal. The value returned by the program is the minimum value of the signal in the water plateau. A more accurate estimate of the minimum could be computed by averaging over a selection of points in the water plateau range. This approach was not used in this work of thesis as we focused on the transition from squeezing regime to dripping regime and not the trasmittivity of the signal. In particular the experiments conducted showed that, as mentioned in the previous chapter, when in pure squeezing regime the voltage signal does not present a clear minimum, but a plateau. When approaching the dripping regime, a clear minimum of the signal can be found. Our interpretation of this phenomenon is that the trend of the minimum can be associated to the shape of the droplet (as explained in the previous chapter). Therefore the study of the minimum of the signal can return useful informations reguarding the geometry of the droplets, making it a parameter of interest for this study.
Fig.4.6-**??** show the values of the minimum of the optical signal plotted as a function of ϕ. The red line corresponds to the power fit: $Min = a \cdot \phi^b + c$:

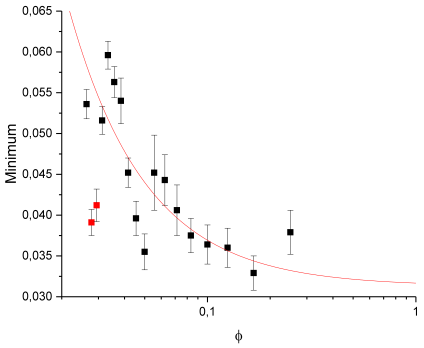

Figure 4.6: Values of the minimum of the signal for $Q_d = 5\mu l/min$ as function of ϕ.

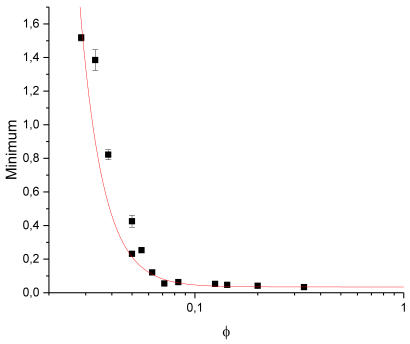

Figure 4.7: Values of the minimum of the signal for $Q_d = 10\mu l/min$ as function of ϕ.

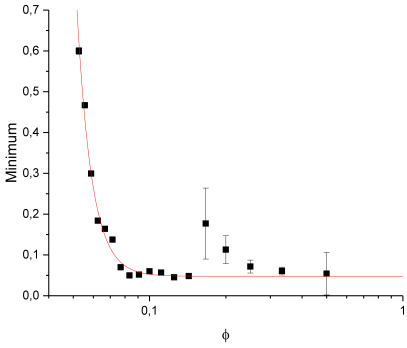

Figure 4.8: Values of the minimum of the signal for $Q_d = 15\mu l/min$ as function of ϕ.

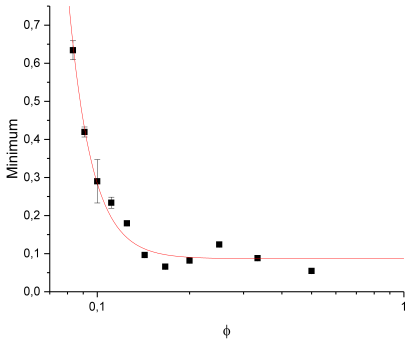

Figure 4.9: Values of the minimum of the signal for $Q_d = 25\mu l/min$ as function of ϕ.

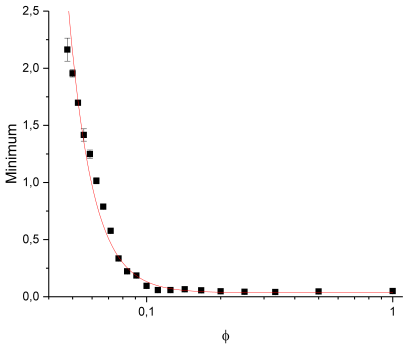

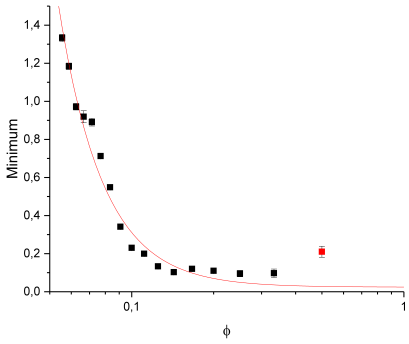

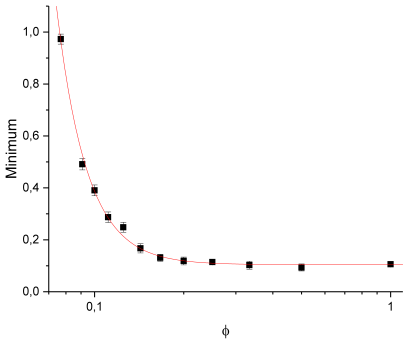

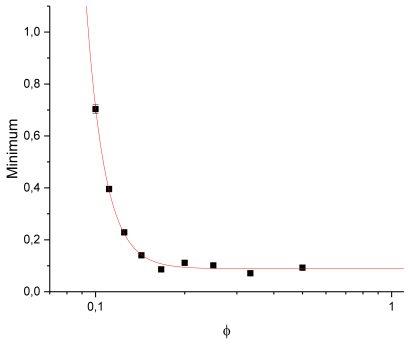

Figure 4.10: Graphs of the minimum of the signal as a function of ϕ for different values of C. **Top left** $C = 0\%$,**Top right** $C = 10\%$,**Bottom left** $C = 25\%$,**Bottom right** $C = 50\%$.

Q_d $[\mu l/min]$	**a**	**b**	**c**
5	$3,767 \pm 0,001$	$0,031 \pm 0,007$	$-1,2 \pm 0,7$
10	$2 \cdot 10^{-6} \pm 2 \cdot 10^{-6}$	$0,034 \pm 0,009$	$-3,9 \pm 0,3$
15	$2 \cdot 10^{-10} \pm 3 \cdot 10^{-10}$	$0,048 \pm 0,006$	$-7,4 \pm 0,6$
20	$4 \cdot 10^{-6} \pm 2 \cdot 10^{-6}$	$0,035 \pm 0,009$	$-4,4 \pm 0,2$
$20 - 10\% glycerol$	$6 \cdot 10^{-4} \pm 5 \cdot 10^{-4}$	$0,02 \pm 0,04$	$-2,6 \pm 0,3$
$20 - 25\% glycerol$	$1,6 \cdot 10^{-5} \pm 7 \cdot 10^{-6}$	$0,104 \pm 0,005$	$-4,2 \pm 0,2$
$20 - 50\% glycerol$	$1 \cdot 10^{-8} \pm 2 \cdot 10^{-7}$	$0,089 \pm 0,007$	$-6,8 \pm 0,8$
25	$1 \cdot 10^{-6} \pm 1 \cdot 10^{-6}$	$0,09 \pm 0,01$	-5, 7 ± 2

Table 4.3: Values of the coefficients of interpolation of the minimum values as a function of $Min = a \cdot \phi^b + c$ for $Q_d = 5, 10, 15, 20, 25$ $\mu l/min$ and $C = 0, 10, 25, 50\%$.

In the table 4.3 the values of the coefficients of the interpolation are reported.

Given the shape of the minimum versus ϕ graph, it is clear that "something" occurred around the knee of the plot. Our deduction is that the knee of the curve is the beginning of the transition from squeezing to dripping regime. The value of the flow rate in the minimum ϕ_{min} was computed interpolating with a line the points at lower flow rate and computing the average value of the minumim for higher flow rates. The intersection between the two lines returns the value of ϕ_{min}.

4.3 Integral

The integral of the signal represents the intensity of the light transmitted by the droplets flow. It is a parameter which depends on the shape of the droplet (in particular it is linked to the curvature of the droplet, as mentioned in the previous chapter) and can always be defined, differently from the minimum, making it a good parameter for the study of the transition.

It was computed for each curve (varying $Q_d = 5, 10, 15, 20, 25\ \mu l/min$ and fixed $Q_d = 20\ \mu l/min$, $C = 0\%, 10\%, 25\%, 50\%$).
In the following the values of the integral as a function of the flow rate ϕ are reported:

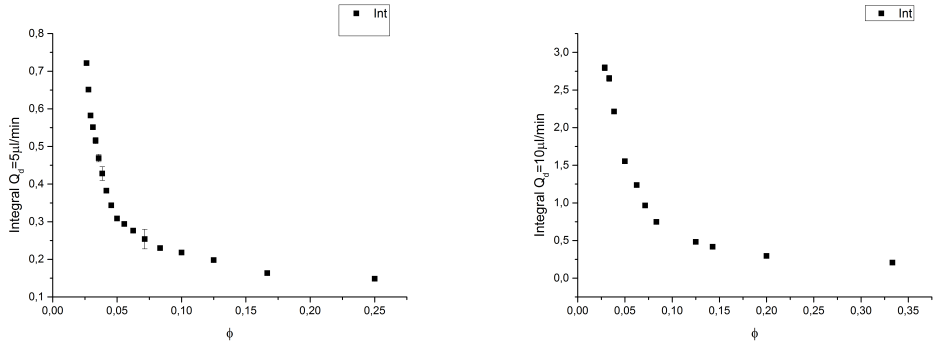

Figure 4.11: Values of the integral of the signal for $Q_d = 5\mu l/min$ (left) $Q_d = 10\mu l/min$ (right) as function of ϕ.

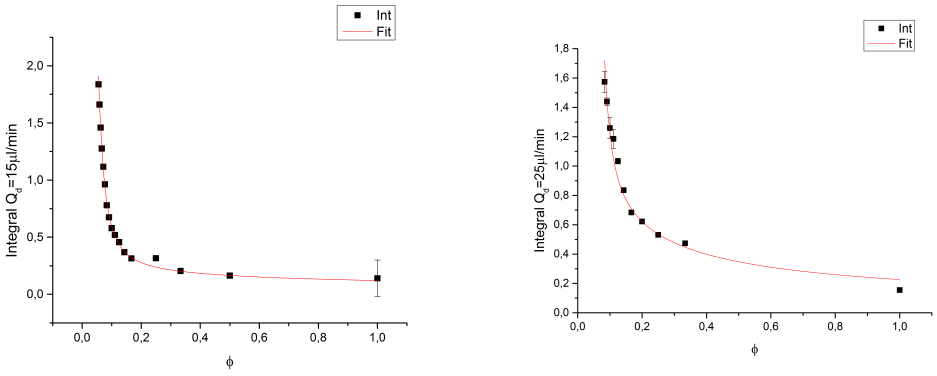

Figure 4.12: Values of the integral of the signal for $Q_d = 15\mu l/min$ (left) and $Q_d = 25\mu l/min$ (right) as function of ϕ.

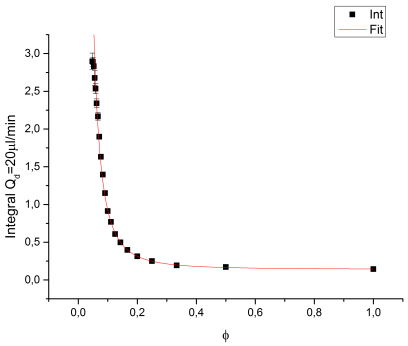

Figure 4.13: Values of the integral of the signal for $Q_d = 20\mu l/min$, $C = 0\%$ as function of ϕ.

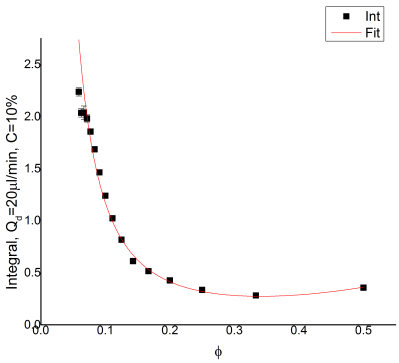

Figure 4.14: Values of the integral of the signal for $Q_d = 20\mu l/min$, $C = 10\%$ as function of ϕ.

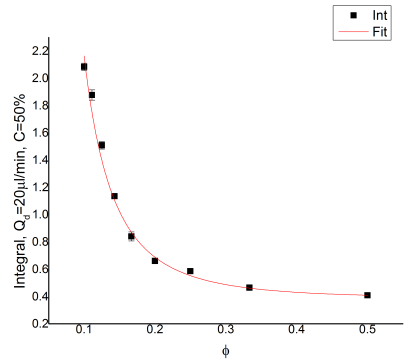

Figure 4.15: Values of the integral of the signal for $Q_d = 20\mu l/min$, $C = 25\%$ as function of ϕ.

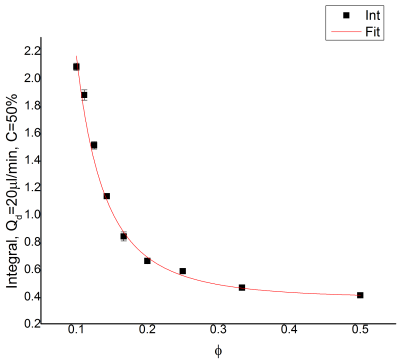

Figure 4.16: Values of the integral of the signal for $Q_d = 20\mu l/min$, $C = 50\%$ as function of ϕ.

The plots follow a trend that is best described by the function $I = a \cdot \phi^b + c \cdot \phi^d$ (red curve in the graphs), differently from the curve of the minimum which followed the single power trend $Min = A \cdot \phi^B + C$. The different behaviour of the parameters can be explained considering the geometrical parameters related to them (as explained in the previous chapter). The minimum of the signal is related to the water plateau: when in squeezing regime the volume occupied by the water is much bigger and the minimum. The integral of the signal, on the other hand, is related to the curvature of the droplet. During the squeezing regime the it is reasonable to assume a different curvature than the squeezing regime. Despite the fact that these results strongly depend on the speed of the droplet the fact that

$Q_d[\mu l/min]$	**a**	**b**	**c**	**d**
5	$3 \cdot 10^{-06} \pm 4 \cdot 10^{-06}$	-3.3 ± 0.4	0.087 ± 0.006	$-0.4 \pm 0.4*$
10	0.018 ± 0.006	-1.47 ± 0.09	0.13 ± 0.03	$0.1 \pm 0.3*$
15	$3 \cdot 10^{-04} \pm 2 \cdot 10^{-04}$	-2.9 ± 0.3	0.12 ± 0.01	-0.4 ± 0.1
20	0.006 ± 0.001	-2.112 ± 0.004	0.140 ± 0.004	$0.02 \pm 0.07*$
$20 - 10\% glycerol$	0.033 ± 0.007	-1.54 ± 0.09	2 ± 1	3 ± 1
$20 - 25\% glycerol$	0.004 ± 0.003	-2.5 ± 0.3	0.24 ± 0.01	$-0.1 \pm 0.2*$
$20 - 50\% glycerol$	0.006 ± 0.01	-2.45 ± 0.7	0.39 ± 0.09	$0.05 \pm 0.5*$
25	$5 \cdot 10^{-06} \pm 5 \cdot 10^{-06}$	-5 ± 3	0.23 ± 0.03	-0.6 ± 0.1

Table 4.4: Values of the coefficient of the double power fit of the integral values as a function of flow rate ratio ϕ. Values maked with * are only qualitative.

The coefficients of the fit for the different experiments are reported in the table **??**.

Again, the shape of the curve indicates the presence of a phenomenon that we identify with the beginning of the transition. Due to the fact that the study of the integral behaviour through the double exponential function would require more experimental data, the study of the two trends of the curve were interpolated with two linear functions. The point ϕ^* where the two lines cross is considered the starting point of the squeezing-dripping transition. The table **??**, shows the values of ϕ^* obtained.

$Q_d[\mu l/min]$	ϕ^*
5	0.058 ± 0.006
10	0.08 ± 0.1
15	0.10 ± 0.01
20	0.113 ± 0.004
$20 - 10\% glycerol$	0.151 ± 0.009
$20 - 25\% glycerol$	0.16 ± 0.01
$20 - 50\% glycerol$	0.164 ± 0.009
25	0.17 ± 0.02

Table 4.5: Values of ϕ^*.

4.4 Asymmetry

Considered the previous analysis on the minimum and the integral of the signal, a third parameter was considered to further study the optical-microfluidic coupling: the symmetry of the droplet. The asymmetry is the most interesting parameter as it relates the integral of the signal to the minimum of the signal and it holds informations reguarding the geometry of the droplet. The left and right integrals of the signal are a convenient tool to measure the symmetry of the droplets produced in the microfluidic channels, as they are directly related to the curvature of the menisci of the droplets. In Fig. **??** an example of the plot of the left and right integrals as a function of ϕ is shown.

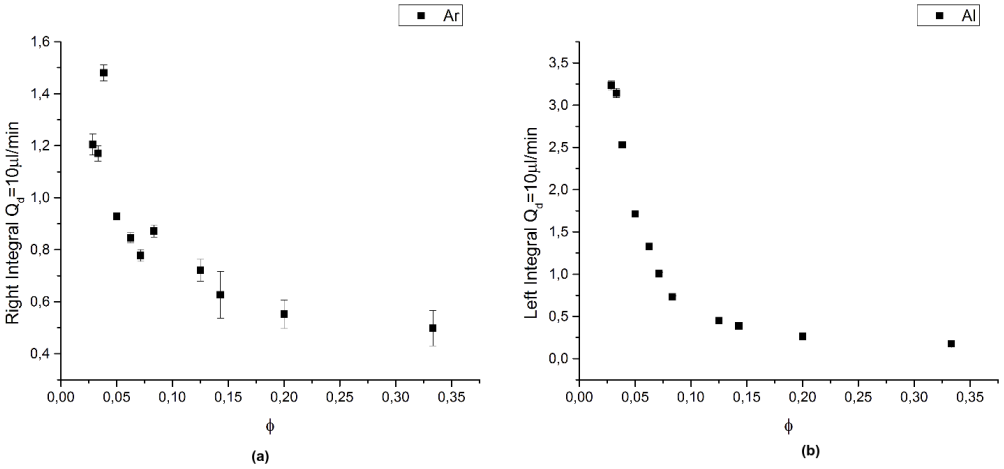

Figure 4.17: $Q_d = 10\ \mu l/min$: (a) Right Integral, (b) left Integral plots as function of ϕ

In particular, instead of using I_{left} and I_{right}, to normalize the results, two adimensional parameters were calculated:

$$\alpha = \frac{I_{right}}{I_{left} + I_{right}}, \qquad \beta = \frac{I_{left}}{I_{left} + I_{right}} \tag{4.1}$$

For each value of Q_d and of glycerol concentration C, these parameters have been studied as a function of the flux rate ϕ. In Fig.**??**-4.19 the plots of $\alpha(\phi)$, $\beta(\phi)$ are reported. It is possible to see that the two parameters have an initial phase where the droplets are highly asymmetric for high flow rates ($\phi \sim 1 \div 0.2$) and tend to symmetry for a certain value of ϕ_{sym}. Due to the instability related to the calculus of the minimum the measure of the

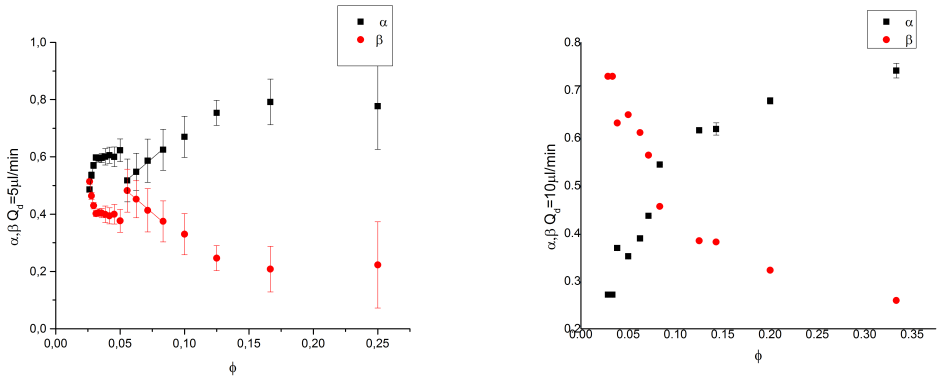

Figure 4.18: Values of the parameters α, β for $Q_d = 10\mu l/min$ (left) and $Q_d = 10\mu l/min$ (right) as function of ϕ.

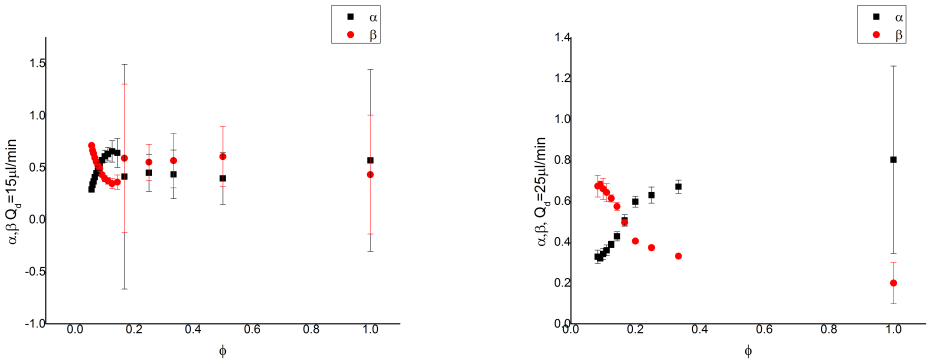

Figure 4.19: Values of the parameters α and β for $Q_d = 25\mu l/min$ (left) and $Q_d = 25\mu l/min$ (right) as function of ϕ.

symmetry for high flow rates is not very accurate.
In order to measure ϕ_{sym} the points in the neighborhood were interpolated with a line as shown in Fig.4.20.

The values of ϕ_{sym} were then compared with ϕ^*. The results are shown in table**??**:

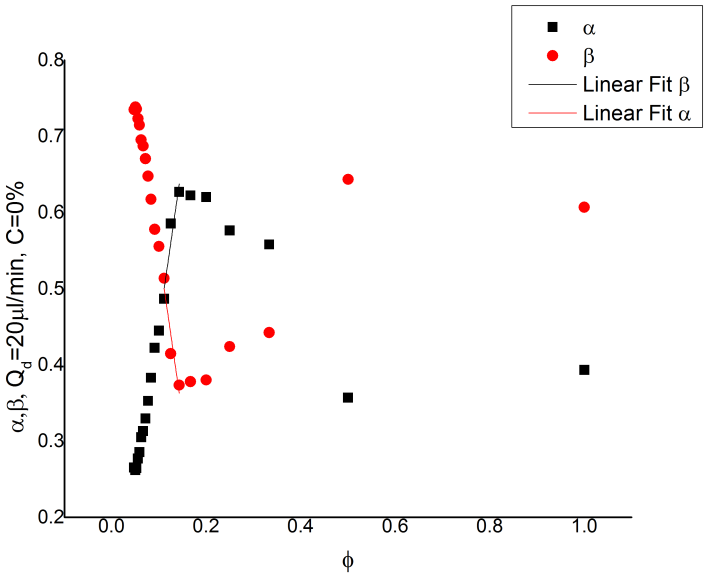

Figure 4.20: Linear fit of α, β. The error bars are not shown in the plot for clarity.

$Q_d[\mu l/min]$	ϕ^*	ϕ_{sym}	ϕ_{min}
5	0.058 ± 0.006	0.048 ± 0.004	0.081 ± 0.009
10	$0.08 \pm 0.1*$	0.08 ± 0.01	0.051 ± 0.008
15	0.10 ± 0.01	0.09 ± 0.01	0.070 ± 0.007
20	0.113 ± 0.004	0.111 ± 0.005	0.11 ± 0.01
$20 - 10\% glycerol$	0.151 ± 0.009	0.152 ± 0.009	0.082 ± 0.008
$20 - 25\% glycerol$	0.16 ± 0.01	0.20 ± 0.03	0.15 ± 0.06
$20 - 50\% glycerol$	0.164 ± 0.009	0.18 ± 0.02	0.15 ± 0.06
25	0.17 ± 0.02	0.17 ± 0.02	0.14 ± 0.04

Table 4.6: Values of ϕ^*, value marked with * is only qualitative.

Some interesting features of ϕ^* are shown in Fig.4.21 and Fig.4.22. Fig. 4.21 shows a linear dependence of the values of the critical flux rate ϕ^* on the dispersed phase flux Q_d, while Fig. 4.22 shows that the value of ϕ^* does not depend on the viscosity rate $\lambda = \frac{\eta_d}{\eta_c}$, where η_d is the viscosity of the dispersed phase[74] and η_c is the viscosity of the continuous phase.

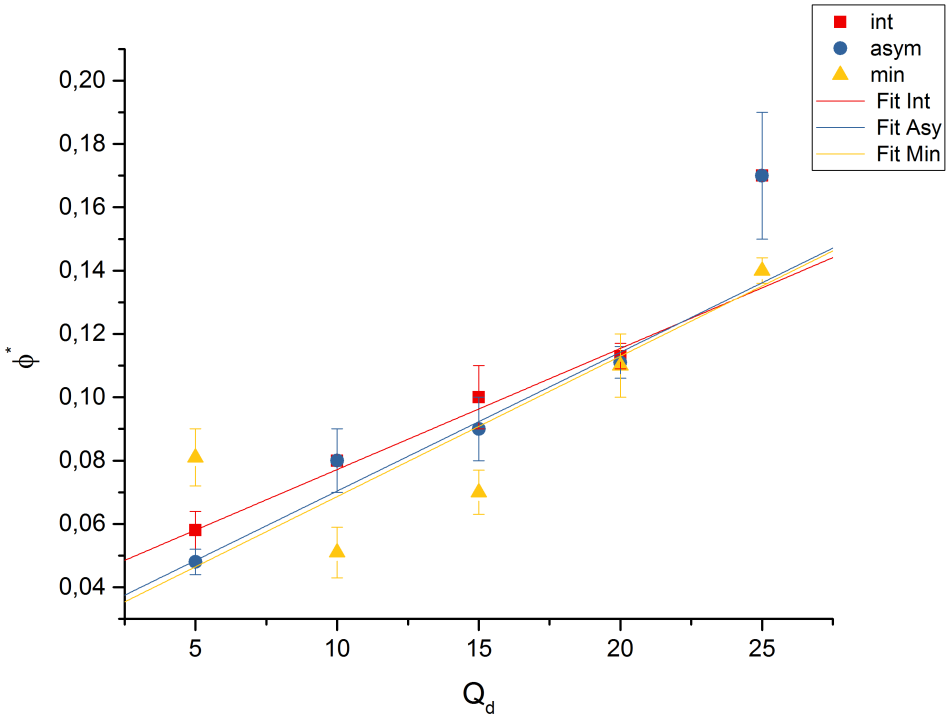

Figure 4.21: Linear dependence of ϕ^* on the dispersed phase flux Q_d.

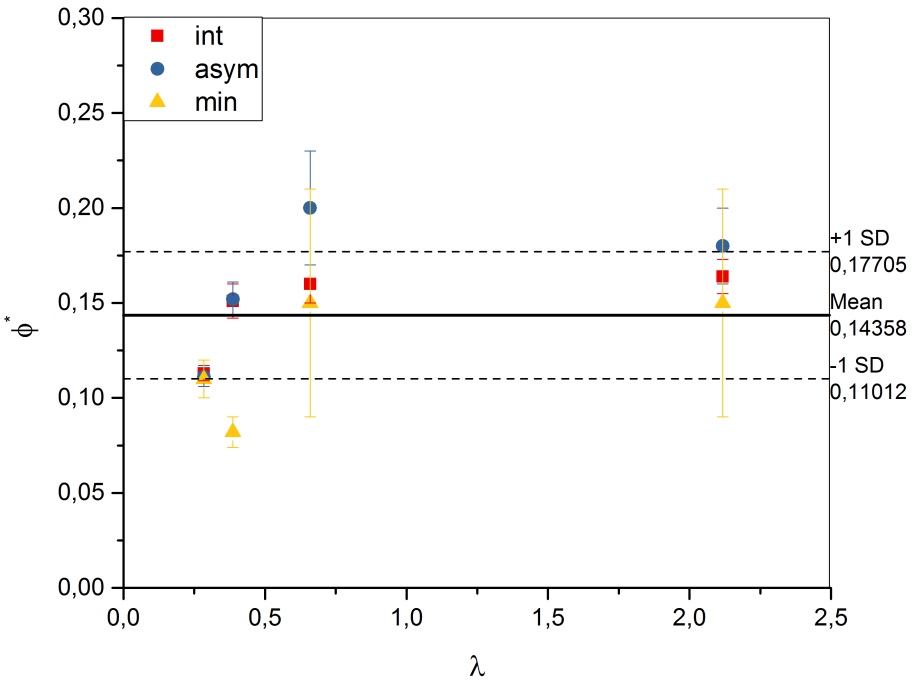

Figure 4.22: Dependence of ϕ^* on λ.

4.5 Capillary Number

An fundamental parameter in microfluidics is the capillary number Ca, defined as:

$$Ca^* = \frac{\eta_c u_c}{\sigma} = \frac{\eta_c Q_c^*}{\sigma h w} \tag{4.2}$$

where $Q_c^* = Q_d/\phi^*$ is the flux of the continuous phase correspondent to ϕ^*, $\sigma = 5\ mN/m$ the superficial tension between the continuous phase and dispersed phase liquids[], $h = 96\ \mu m$ the height of the channel, $w = 201\ \mu m$ the width of the channel and η_d is the viscosity of the dispersed phase (for $T = 27\ ^oC$). In particular the value of the viscosity for the continuous phase (hexadecane with SPAN 80) is $\eta_c = 0.003\ Ns/m^2$. The table 4.6 shows the values of the capillary number with the respect to Q_d.

$Q_d[\mu l/min]$	Ca^*_{int}	Ca^*_{min}	Ca^*_{asym}
5	0.046 ± 0.005	0.032 ± 0.004	0.054 ± 0.005
10	0.066 ± 0.008	0.10 ± 0.02	0.065 ± 0.008
15	0.079 ± 0.008	0.11 ± 0.01	0.086 ± 0.009
20	0.094 ± 0.003	0.090 ± 0.009	0.094 ± 0.004
25	0.078 ± 0.009	0.093 ± 0.003	0.076 ± 0.009

Table 4.7: Values of Ca^* calculated for distilled water.

In literature [20][18][14], typical values of Ca in the squeezing and dripping regime are:

$$0.013 < Ca_{Dripping} < 0.1 \qquad Ca_{Squeezing} < 0.0058 \tag{4.3}$$

According to these values the results of the measure of the Ca would indicate that the regime of the droplets would be the dripping regime. That is clearly not the case of the droplets used in this work of thesis, we can be certain of this due to the shape of the droples that was verified with the images taken with the fast camera. This discrepancy is probably due to the fact that the estimate of the velocity u_{drop} of the droplet computed in this work of thesis is given by the formula:

$$u_{drop} = \frac{Q_c*}{hw} \tag{4.4}$$

which is not a good parameter because the continuous phase velocity is different from the droplets velocity due to the presence of gutters around the droplets. Neverless,the possibility to optically study the transition allows future studies and outlooks on the use of optical parameters, such as the ones described in this work to further investigate the microfluidic droplets behaviour.

It is interesting to notice the linear dependence of the capillary number as a function of the dispersed phase flux Q_d shown in figure.

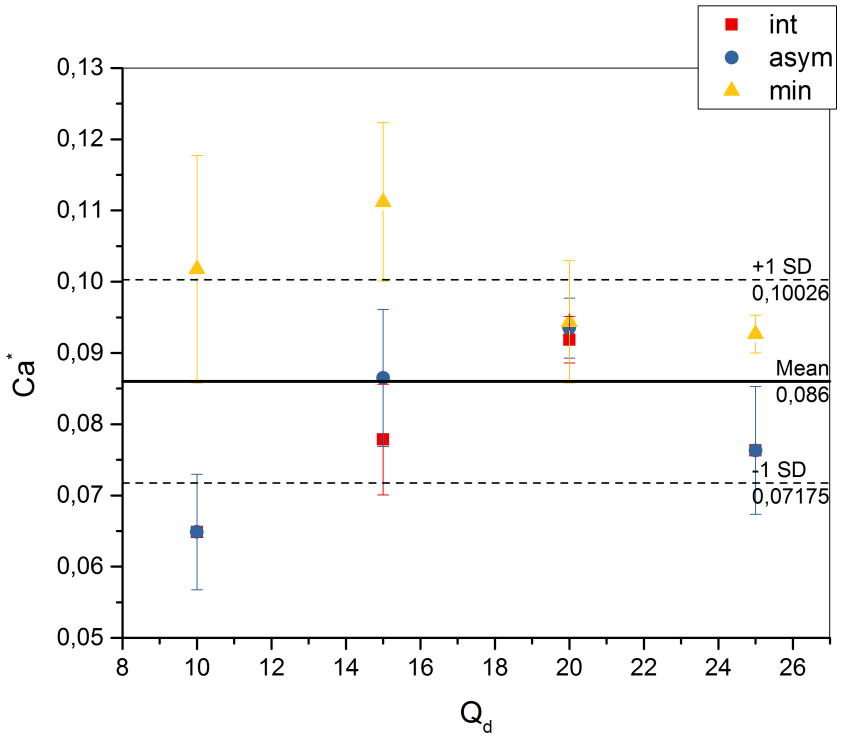

Figure 4.23: Values of Ca^* as function of the dispersed phase value Q_d.

Conclusions

The aim of this work of thesis was the study of an optofluidic chip.
In particular the main objective was to relate optical parameters to physical properties of the droplets generated inside the chip.
The first step was the realization of the optofluidic chip itself. The chip was entirely integrated on lithium niobate, titanium in-diffused waveguides were coupled effectively to microfluidic channels. An investigation of the quality of the waveguides was conducted my means of a near-field set up. The study was conducted for both TE an TM mode in order to verify wether the incident beam mode had an impact on the propagation of the light inside of the waveguide. No significant differences were noticed between the two modes.
The second part of the thesis saw the realization of water-in-oil droplets inside the chip, in a T-junction configuration. In particular the experiment consisted in varying the flow of the continuous phase while keeping fixed the flow of the dispersed phase.
Different solutions of glycerol-in-water were prepared as a dispersed phase in order to study the response of the system as a function of the viscosity.
The optical signal was recorded with a photodiode while the images of the droplets were simultaneously recorded with a fast camera Basler acA800-510um. The optical signal was studied my means of an ad-hoc written software which computed:

1. The integral of the signal. This parameter indicates the intensity of the radiation collected by the photodiode and returns a value which is linked to the curvature of the droplet. In particular the signal of the integral as a function of the flow rate exibits a double power trend.

2. The minimum of the signal, which is related to the trasmittivity of the device and can be used to obtain useful informations reguarding the shape of the droplet. The trend exhibited by the minimum of the signal as a function of the flow rate was a power trend.

3. The time the droplet takes to pass in front of the waveguide, which gives an estimate of the length of the droplet. Once the length of the

droplet and its velocity are known it is possible to compute the volume of the droplet which is a very important parameter in microfluidics. From the study of the length of the droplet some interesting facts have emerged:

- the droplet length as a function of ϕ follows a power law differenctly from the predictions found in literature[18][20] where a linear dependence was claimed.
- the droplet velocities depend strongly on the dispersed phase flux for larger droplets but tend to the same velocity for smaller droplets.

4. The left integral and right integral of the signal which are related to the curvature of the droplet (they are associated to the curvature of the left and right meniscus respectively). These parameters are useful to verify the symmetry of the droplet by means of adimentional parameters α, β.

In particular the experiments were carried out in the squeezing regime and in squeezing to dripping regime.
The optical analysis allowed to find a value ϕ^* of the flow rate ϕ, common to all the parameters, in which the trend of the parameter changes. This value ϕ^* could be interpreted as the beginning of the transition from the squeezing to dripping regime, but further studies must be carried out to verify this interpretation.
In particular the data showed a linear dependence of the parameter ϕ^* on the value of the dispersed phase flux Q_d.
The results obtained in this work of thesis, alongside with the ones obtained by our group [16][17] are proof of the validity of the set-up used to create Lab-on-Chip devices.

Bibliography

[1] Volk T and Wöhlecke M, *Lithium niobate: defects, photorefraction and ferroelectric switching* , vol. 115 (Springer Science & Business Media, 2008).

[2] Lerner P, Legras C and Dumas J (1968) *Stoechiometrie des monocristaux de metaniobate de lithium. Journal of Crystal Growth* , vol. 3:pp. 231–235.

[3] Sohler W, Dibyendu D, Selim R et al. (2005) *Erbium-doped lithium niobate waveguide lasers.* IEICE transactions on electronics, **vol. 88, no. 5** :pp. 990–997.

[4] Wohlecke M, Corradi G and Betzler K (1996) *Optical methods to characterise the composition and homogeneity of lithium niobate single crystals.* Applied physics B, **vol. 63, no. 4**:pp. 323–330.

[5] Luennemann M, Hartwig U, Panotopoulos G et al. (2003) *Electrooptic properties of lithium niobate crystals for extremely high external electric fields.* Applied Physics B, **vol. 76, no. 4**:pp. 403–406.

[6] Bernal E, Chen G and Lee T (1966) *Low frequency electro-optic and dielectric constants of lithium niobate.* Physics Letters, **vol. 21, no. 3**:pp. 259–260.

[7] Du XY, Swanwick ME, Fu YQ et al. (2009) *Surface acoustic wave induced streaming and pumping in 128 Y-cut LiNbO 3 for microfluidic applications.* Journal of Micromechanics and Microengineering, **vol. 19, no. 3**:p. 35016

[8] Shi J, Mao X, Ahmed D et al. (2008) *Focusing microparticles in a microfluidic channel with standing surface acoustic waves (SSAW).* Lab on a Chip, **vol. 8, no. 2**:pp. 221–223.

[9] Weis R and Gaylord T (1985) *Lithium niobate: summary of physical properties and crystal structure.* Applied Physics A, **vol. 37, no. 4**:pp. 191–203.

[10] Grilli S and Ferraro P (2008) *Dielectrophoretic trapping of suspended particles by selective pyroelectric effect in lithium niobate crystals.* Applied Physics Letters, **vol. 92, no. 23**:p. 232902.

[11] FerraroP, CoppolaS, GrilliS et al. (2010) *Dispensing nano-pico droplets and liquid patterning by pyroelectrodynamic shooting.* Nat Nano, **vol. 5, no. 6**:pp. 429–435.

[12] Glass A, Von der Linde D and Negran T (1974) *High-voltage bulk photovoltaic effect and the photorefractive process in LiNbO3.* Applied Physics Letters, textbfvol. 25, no. 4:pp. 233–235.

[13] Griffiths GJ and Esdaile RJ (1984) *Analysis of titanium diffused planar optical waveguides in lithium niobate.* Quantum Electronics, IEEE Journal of, **vol. 20, no. 2**:pp. 149–159.

[14] De Menech M, Garstecki P, Jousse F et al.(2008)

Transition from squeezing to dripping in a microfluidic T-shaped junction Journal of Fluid Mechanics, **vol. 595**:pp. 141–161.

[15] Bettella G. (2016) *Integrated Opto-Microfluidic Lab-on-a-Chip in Lithium Niobate for Droplet Generation and Sensing*, Phd thesis.

[16] Garbellotto L. (2017) *Integrated opto-microfluidic platform in $LiNbO_3$ crystals toward a new conceptof miniaturized microphotometry.*, Master Thesis.

[17] De Bortoli L. (2017) *Study of light-driven phenomena in integrated opto-microfluidic lithium niobate platforms*, Master thesis.

[18] Garstecki P, Fuerstman J M, Stone A H, Whitesides G M. (2006) *Formation of droplets and bubbles in a microfluidic T-junction scaling and mechanism of break-up.* Lab Chip, 6(3):437-446

[19] Cortés-Estrada A.H., Ibarra-Bracamontes L.A., Aguilar-Corona A., Viramontes-Gamboa G., Carbajal-De la Torre G. (2014) *Surface Tension and Interfacial Tension Measurements in Water-Surfactant-Oil Systems Using Pendant Drop Technique.* In: Klapp J., Medina A. (eds) Experimental and Computational Fluid Mechanics. Environmental Science and Engineering. Springer, Cham

[20] Gordon F Christopher, N Nadia Noharuddin, Joshua A Taylor, and Shelley L Anna.(2008) *Experimental observations of the squeezing-to-dripping transition in t-shaped microfluidic junctions.* Physical Review E, 78(3):036317.

[21] E.K. Sackmann Et Al. "The Present And Future Role Of Microfluidics In Biomedical Research" Nature Vol.507 N.7491 pp.181-9 (2014)

[22] A. Liga Et Al. "*Exosome Isolation: A Microfluidic Road-Map*" Lab Chip Vol.15 P.2388-2394 (2015)

[23] Daiying Zhang Et Al. *Microfabrication And Applications Of Opto-Microfluidic Sensors* Sensors Vol.11 Pp.5360-5382 (2011)

[24] D. Psaltis Et Al. Nature Vol. 442 P-381-386 (2006)

[25] Kin Fong Lei *Microfluidic Systems For Diagnostic Applications: A Review* Journal Of Laboratory Automation XX(X) Pp.1–18 (2012)

[26] G. Gauglitz "Point-Of-Care Platforms" Annual Review Of Analytical Chemistry Vol. 7: 297-315 (2014)

[27] Jong-Ryul Choi Et A. "Microfluidic Assay-Based Optical Measurement Techniques For Cell Analysis: A Review Of Recent Progress" Biosensors And Bioelectronics Vol.77 pp 227-236 (2016)

[28] J.P. Mcmullen Et Al. Annu. Rev. Anal. Chem. V.3 P.19-42 (2010)

[29] S. Y. Teh Et Al. Lab Chip V.8 pp 198-220 (2008)

[30] P. Abgrall And A-M Gue *Lab-On-Chip Technologies: Making A Microfluidic Network And Coupling It Into A Complete Microsystem—A Review* J. Micromech. Microeng. 17 R15–R49 (2007)

[31] H.A. Stone *Engieneering flow in small devices. Microfluidics toward a Lab On A Chip* Annual Review Of Fluid Mechanics Vol. 36: 381-411 (Volume Publication Date January 2004)

[32] P. Watts Et Al. Chem. Soc. Rev. 34, 235-246 (2005)

[33] C. Monat et al. *Integrated Optofluidics: A New River of Light* Nature Photonics Vol1. pp 106-114 (2007)

[34] P. Neuzil et al.

[35] V.Srinivasan Et Al. " An Integrated Digital Microfluidic Lab-On-A-Chip For Clinical Diagnostics On Human Physiological Fluids", Miniaturisation For Chemistry, Biology & Bioengineering Lab Chip Vol4 , 310–315 (2004)

[36] L. Pang *Optofluidic Devices And Applications In Photonics*, Sensing and imaging Lab Chip,2012,12, 3543-35551 DOI:10.1039/C2LC40467B

[37] J. Guck Et Al, Biophys. J. Vol.81 p.767 (2001)

[38] E. Ananthakrishnan Et Al, J. Theoret. Biology 242, 502 (2006)

[39] B. Lincoln Et Al, Biomed. Microdevices vol.9 p.703 (2007)

[40] P. Cicuta Et Al, Soft Matter vol.3 p.1449 (2007)

[41] M. Radmacher, Methods Cell Biol. Vol.68 p.67 (2002)

[42] N. Wang Et Al, Science vol.260 p.124 (1993)

[43] J.C. Baret Et Al. Med Sci vol.25(6-7) pp627-32 (2009)

[44] DN. Breslauer Et Al, Mol. Biosyst. Vol.2 p.97 (2006)

[45] CE.Sims et al, Lab Chip vol.7 p.423 (2007)

[46] N. Ye Et Al, Lab Chip vol.7 p.696 (2007)

[47] LJ. Blackwell Et Al, Methods Mol. Biol. Vol.565 p.225 (2009)

[48] G. Testa Et A. "A Hydrid Silicon-PDMS Optofluidic Platform For Sensing Application" Biomedical Optics Express Vol.14 N.2 P.417 (2014)

[49] F. Bragheri Et Al, J. Biophotonics vol.3 p.234 (2010)

[50] N. Bellini Et Al, Opt. Express vol.18 p.4679 (2010)

[51] R. Gattass Et Al, Nat. Photonics vol.2 p.219 (2008)

[52] G. Della Valle, J. Opt. A: Pure Appl. Opt. Vol.11 p.013001 (2009)

[53] V. Maselli Et Al, Appl. Phys. Lett. Vol.88 p.191107 (2006)

[54] R. Osellame Et Al, Appl. Phys. Lett. Vol.90 p.231118 (2005).

[55] V. Chokkalingam er al., Lab Chip, Vol.10 p.1700 (2010)

[56] P. Watts Et Al. Chem. Soc. Rev. Vol. 34 P.235-246 (2005);

[57] K. Jensen Et Al. Lab Chip Vol.4, P.31 (2004)

[58] R. B. Fair, Micro. Nanofluidics Vol.3, P. 245-281 (2007)

[59] G. F. Christopher Et Al. J. Phys. D 40, R319-R336 (2007)

[60] R. B. Fair, Micro. Nanofluidics Vol.3, P. 245-281 (2007)

[61] C. Baraurd et al. Lab On Chip 7:1029-1033. (2007)

[62] J.C. Baret Et Al. Med Sci. Vol.25(6-7) pp.627-32 (2009)

[63] M. Sin Et Al Jour. Biol. Eng. Vol.5 P.1-21 (2011)

[64] J. Friend Et Al. Rev. Of Modern Physics Vol.83 P. 647-704 (2011)

[65] M.Bazzan And C. Sada *Optical Waveguides In Lithium Niobate: Recent Developments And Applications*, Appl. Phys. Rev.2, 040603(2015)

[66] T. Volk Et Al., Lithium Niobate Defects, *Photorefraction And Ferroelectric Switching*, Springer Ed., ISBN 978-3-540-70765-3, Berlin(2008)

[67] G. Pozza et al. *Optofluidics, Microfluidics and Nanofluidics* Vol.1 n.1 p.2300-7435 (2014)

[68] L. Stern Et Al. *Doppler Based Flow Rate Sensing In Microfluidic Channels* Sensors, Vol.14 p. 16799 (2014)

[69] K. V.I. Kaler *Droplet Microfluidics For Chip Based Diagnostic*, Sensors Vol.14 p.23283 (2014)

[70] B.S. Lin (2014) *A PDMS-Based Cylindrinc Hydrid Lens For Enhanced Fluorescence Detection In Microfluidic Systems* Sensors Vol.14 p.2967

[71] Chauvet M et al.*Integrated Optofluidic Index Sensor Based on Self-Trapped Beams in LiNbO3*Al. APL Vol.101 p.181104 (2012)

[72] M. Esseling Et Al. Optics Express vol.18 pp17404-17411 (2010)

[73] N.C. Carville et al. *Biocompatibility of ferroelectric lithium niobate and the influence of polarization charge on osteoblast proliferation and function.* J. Biomed Mater. Res. A vol.103(8) pp.2540-8 (2015)

[74] Cheng (2008) Ind. Eng. Chem. Res.47 3285-3288